High-fidelity Reaction Kinetic Modeling of Hot-Jupiter Atmospheres Incorporating Thermal and UV Photochemistry Enhanced by Metastable CO (a3Π)

Jeehyun Yang, Murthy Gudipati, Bryana Henderson, Benjamin Fleury

The Astrophysical Journal, 947:26 (30pp), 2023 April 10 https://doi.org/10.3847/1538-4357/acbd9b

High-fidelity Reaction Kinetic Modeling of Hot-Jupiter Atmospheres Incorporating Thermal and UV Photochemistry Enhanced by Metastable CO($a^3\Pi$)

Jeehyun Yang[1], Murthy S. Gudipati[1], Bryana L. Henderson[1], and Benjamin Fleury[2]
[1] Science Division, Jet Propulsion Laboratory, California Institute of Technology, 4800 Oak Grove Drive, Pasadena, CA 91109, USA; murthy.gudipati@jpl.nasa.gov, jeehyun.yang@jpl.nasa.gov
[2] Université Paris Est Créteil and Université Paris Cité, CNRS, LISA, F-94010 Créteil, France
Received 2022 October 6; revised 2023 January 12; accepted 2023 February 16; published 2023 April 14

Abstract

A detailed modeling of simultaneous UV-photochemical and thermochemical processes in exoplanet atmosphere-like conditions is essential for the analysis and interpretation of a vast amount of current and future spectral data from exoplanets. However, a detailed reaction kinetic model that incorporates both UV photochemistry and thermal chemistry is challenging due to the massive size of the chemical system as well as the lack of understanding of photochemistry compared to thermal-only chemistry. Here, we utilize an automatic chemical reaction mechanism generator to build a high-fidelity thermochemical reaction kinetic model later then incorporated with UV photochemistry enhanced by metastable triplet-state carbon monoxide ($a^3\Pi$). Our model results show that two different photochemical reactions driven by Lyα photons (i.e., $H_2 + CO(a^3\Pi) \rightarrow H + HCO$ and $CO(X^1\Sigma^+) + CO(a^3\Pi) \rightarrow C(^3P) + CO_2$) can enhance thermal chemistry resulting in significant increases in the formation of CH_4, H_2O, and CO_2 in H_2-dominated systems with trace amounts of CO, which qualitatively matches the observations from previous experimental studies. Our model also suggests that at temperatures above 2000 K, thermal chemistry becomes the dominant process. Finally, the chemistry simulated up to 2500 K does not produce any larger species such as C_3 species, benzene, or larger (i.e., PAHs). This might indicate that the photochemistry of C_2 species such as C_2H_2 might play a key role in the formation of organic aerosols observed in a previous experimental study.

Unified Astronomy Thesaurus concepts: Exoplanet atmospheres (487); Exoplanet atmospheric composition (2021); Theoretical models (2107); Hot Jupiters (753); Planetary atmospheres (1244); Astrochemistry (75)

Supporting material: tar.gz file

1. Introduction

With increasing detection of exoplanets and spectroscopic characterization of exoplanet atmospheres, our knowledge of other stellar systems and planets around these stars is expanding significantly. Many of the spectral exoplanet transmission data are from the atmosphere of hot Jupiters and giant planets with short orbital periods and small semimajor axis values, which indicates that both thermal equilibrium chemistry and UV photochemistry are available in these hot-Jupiter atmospheres (Moses 2014; Madhusudhan et al. 2016), and hence simultaneous thermal and photochemical reaction pathways need to be considered when modeling the atmospheric composition of these UV-rich hot-Jupiter-like exoplanets. It has been suggested from previous theoretical studies that thermal chemistry mainly dominates hot-Jupiter atmospheres with temperatures above 1500 K, while disequilibrium chemistry such as photochemistry could play an important role in exoplanet atmospheres whose temperatures are lower than 1500 K (Moses et al. 2011; Venot et al. 2012; Moses 2014).

The chemistry of an exoplanetary atmosphere largely depends on its C/O ratio, where C/O $\geqslant$ 1 indicates a carbon-rich atmosphere and C/O $<$ 1 indicates an oxygen-rich atmosphere (solar C/O = 0.5). Along with temperature, these C/O ratios can be used to classify exoplanetary atmospheres and identify the major chemistry products that occur in each case. Several groups have explored the connection between C/O ratio, temperature, and chemistry in the hot-Jupiter atmospheres using modeling, observations, and experiments, including those of Madhusudhan (2012), Moses et al. (2013), Venot et al. (2015), Drummond et al. (2019), and Fleury et al. (2019, 2020). Madhusudhan (2012) combined observations with an atmospheric chemical model (photochemistry not included) to classify how the C/O ratio affects the chemical compositions of the atmospheres, and using a 1D thermo-photochemical model, Venot et al. (2015) explored how various parameters including the C/O ratio affect the chemistry in hot-Jupiter atmospheres. Fleury et al. (2019, 2020) experimentally explored the influence of the C/O ratio on the formation of trace species and photochemical aerosols in hot-Jupiter atmospheres.

Among these, the experimental studies by Fleury et al. (2019, 2020) clearly showed enhanced formation of CH_4, H_2O, and CO_2 through simultaneous thermal and UV photochemistry compared to the product formation with thermal-only chemistry at the temperature conditions below 1500 K. They also observed the formation of nonvolatile hydrocarbon aerosols as solid thin films after the UV irradiation of carbon-enriched (C/O = 1) gas mixture at the temperature of 1473 K (Fleury et al. 2019).

These two previous experimental studies provided us with new and first experimental insights into the potential importance of photochemistry in hot-Jupiter-like exoplanet atmospheres as well as interesting questions with regard to the

formation pathways for both observed gaseous products (i.e., CH_4, H_2O, and CO_2) and aerosol products. By tracking these formation pathways for both gaseous and condensed-phase products from laboratory experimental data points, we can identify key chemical species including intermediates that are formed during UV irradiation of the laboratory analogs of exoplanet atmospheres. Eventually, these reactions can be implemented into a 1D *T*–*P* profile supported atmospheric photochemical models (also known as atmospheric photochemical models) that address various physical (e.g., vertical diffusion of molecules, dry and wet deposition, atmospheric escape, condensation and sedimentation of species, etc.) and chemical (e.g., photochemistry, kinetics of the reactions between atmospheric components, etc.) principles (Hu et al. 2012). Adding a more complete picture of reaction chemistry into this atmospheric photochemical model will benefit the analysis and interpretation of a vast amount of current and future spectral data from exoplanets as well as designing future space missions.

For example, the combination of the recent observational data of the atmosphere of WASP-39b by JWST and the atmospheric chemical modeling works has suggested the first evidence of photochemistry in an exoplanet atmosphere (Tsai et al. 2022). Indeed, the JWST observational data of the atmosphere of WASP-39b shows a peak at 4.05 μm that has been attributed to SO_2 molecules. Using multiple atmospheric photochemical model results, Tsai et al. (2022) strongly suggest that SO_2 is formed by photochemistry in the atmosphere of WASP-39b after tracking its formation pathways using reaction kinetic modeling. Therefore, it is clear that photochemistry plays an important role in the composition and spectra of observed exoplanet atmospheres, providing the rationale that precise reaction kinetic modeling is essential when it comes to atmospheric photochemical modeling. When this precise reaction kinetic modeling is coupled with experimental work as presented in this study, it can significantly benefit the astronomical community by decreasing uncertainties in chemical reactions that need to be implemented in atmospheric chemical models used to interpret observational data.

Tracking chemical formation pathways of laboratory experiments is very challenging without the aid of reaction kinetic modeling. This is because the timescales of the initial chemical reactions are too short even for the well-controlled pseudo-first-order radical chemistry (e.g., $\sim$30 μs) (Golan et al. 2013), so that the products that are observed in gas-phase static cell experiments (e.g., Fleury et al. 2019, 2020) are formed far beyond tertiary or even further reaction chemistry (including surface chemistry on the wall). For this reason, reaction kinetic modeling has been actively utilized in a variety of fields (e.g., astrochemistry, combustion research, etc.) to interpret various observational and experimental data. Particularly, the advancement of computer-aided automatic construction of reaction kinetic modeling in combustion research is impressive. For example, Liu et al. (2020) used the Reaction Mechanism Generator (RMG; Gao et al. 2016; Liu et al. 2021) to automatically construct the acetylene pyrolysis model (with a temperature range of 1000–1500 K, a pressure of 0.2 atm, and a reaction time of 0.5 s) that contains 1594 species and 8924 reactions and successfully described pyrene formations observed from the previous acetylene (C_2H_2) pyrolysis experiment by Norinaga et al. (2008).

RMG is an open-source software that automatically constructs networks with relevant core reactions based on its own algorithm to choose reaction rates (e.g., experimentally measured rates would be prioritized followed by less reliable sources in order) and a rate-based iterative algorithm for model generation (Gao et al. 2016). This approach has a few advantages over the traditional way (i.e., manually choosing reaction rates from previous references) of building reaction chemical networks: (i) since reaction rates are chosen based on a rate-based iterative algorithm, compared to manually selecting reaction rates, it is less likely that the reaction mechanism will miss important (i.e., relevant) reactions as long as the reaction libraries are solid, (ii) the approach has multiple self-feedback and refinement steps that are based on a solid algorithm, thus providing the model with more reliability, and (iii) this automatic approach enables us to describe larger and more complex chemical systems that cannot be constructed in the traditional way.

As we can see from Liu et al. (2020)'s C_2H_2 pyrolysis model, in order to reasonably describe the chemistry of exoplanet atmosphere-like conditions (i.e., T = 1000–1500 K and P = 0.2 atm) with even relatively simple starting material (i.e., C_2H_2), a model size is required that is too enormous to construct manually. This enormous model size gives us a rationale to utilize this computer-aided modeling technique to precisely interpret experimental studies of hot-Jupiter atmospheric chemistry.

In addition, including photochemistry in reaction kinetic modeling is also important. Although the temperature, pressure, and chemical conditions of hot-Jupiter atmospheres are similar to those of flames (i.e., combustion), the existence of UV photons (mainly Lyα from their parent stars) in hot-Jupiter atmospheres is the major difference that distinguishes hot-Jupiter atmosphere from combustions (France et al. 2013; Miguel et al. 2015). Molecules in the top layers of hot-Jupiter atmospheres will interact with accessible UV photons and contribute to the whole reaction chemistry of the system. Among a variety of molecules available in hot-Jupiter atmospheres, carbon monoxide (CO) is one of major interest to astrochemists since CO is predicted to be one of the most abundant species in hot-Jupiter-type exoplanet atmospheres whose temperatures are higher than 1000 K (Moses et al. 2013; Venot et al. 2015; Drummond et al. 2019).

Additionally, the recent laboratory experimental results by Fleury et al. (2019, 2020) strongly suggest CO as a possible photochemical precursor driven by CO photoexcitation, but lacked a detailed reaction kinetic model to explain reaction pathways to the observed products. Indeed, CO can be electronically excited to remain chemically reactive with a relatively long lifetime through UV irradiation (Fournier et al. 1980; Gudipati & Kalb 1998; Lee et al. 2020). Although photochemically excited CO has been raised as an important precursor to photochemical pathways (Fleury et al. 2019; Roudier et al. 2021), as far as we know, no previous study has ever assessed the reaction kinetic role of this electronically excited CO in these hot-Jupiter-like atmospheres in detail.

With this background, we will utilize an automatic chemical reaction mechanism generator to build a high-fidelity chemical network that can assess the chemical importance of photo-excited carbon monoxide and qualitatively rationalize the increase in the production yields of CH_4, H_2O, CO_2, and aerosols during UV irradiation compared to thermal-only

chemistry, which has been observed in previous studies by Fleury et al. (2019, 2020). Our work reported here is the first of its kind to incorporate simultaneous thermally and photochemically excited CO-induced chemical reaction pathways, which will provide not only a better insight into reaction mechanisms in hot-Jupiter like exoplanet atmospheres, but also provide a tool to confidently predict major and minor atmospheric molecular species under different conditions.

2. Methods

2.1. Kinetic and Thermodynamic Parameter Libraries

In order to consider the conversion of carbon monoxide into methane, part of the kinetic and thermodynamic parameters were taken from a recent experiment, and kinetic modeling combined the study of methane oxidation by Hashemi et al. (2016) and chosen as the seed mechanism's kinetic parameters that are included in the reaction kinetic model as the main chemistry. All the other kinetic and thermodynamic parameters were taken from the libraries included in the previous acetylene pyrolysis model by Liu et al. (2020) that successfully described up to pyrene (4-ring polycyclic aromatic hydrocarbons) formation observed from the previous experiment by Norinaga et al. (2008) starting from acetylene for the residence time of 0.5 s at the temperatures of 1073–1373 K, at the pressure of 80 mbar. In doing so, we can describe any larger molecules that might have been formed but not observed in the previous experiments by Fleury et al. (2019) and Fleury et al. (2020). All these kinetic and thermodynamic parameters can be found in CHEMKIN format in the supplementary .tar.gz package. With regard to thermodynamic parameters of the triplet carbon monoxide (i.e., $CO(a^3\Pi)$) that is not available in the library (since RMG's library usually contains the thermodynamic parameters of molecules in the ground state), we first carried out electronic structure calculations at the CBS-QB3 level of theory using Gaussian 09 (Frisch et al. 2009) to determine geometric conformations, energies, and vibrational frequencies of the triplet carbon monoxide. Then the thermodynamic parameters of this molecule were calculated by Arkane (Allen et al. 2012), a package included in the open-source software RMG v3.1.0 (Gao et al. 2016; Liu et al. 2021), with atomic energy corrections, bond corrections, and spin–orbit corrections, based on the CBS-QB3 level of theory as the model chemistry. These thermodynamic parameters of the triplet carbon monoxide is given in CHEMKIN format in the supplementary .tar.gz package as well as molecular parameter outputs (Gaussian 09 output file) and the Arkane input file.

2.2. Automatic Generation of the Thermochemical Reaction Network

RMG was used to generate the thermal chemistry model that can simulate the experiments of Fleury et al. (2019, 2020). An initial molar composition of 99.7% of hydrogen and 0.3% of carbon monoxide was used for the experimental condition of Fleury et al. (2019), while an initial molar composition of 99.26% of hydrogen, 0.26% of carbon monoxide, and 0.48% of water was used for the experimental condition of Fleury et al. (2020). Batch reactor conditions were set with a temperature range of 300–1800 K and a pressure of 15 mbar for both models. These physical conditions are relevant to the atmosphere of hot Jupiters and gas giant exoplanets. For example, according to Tsai et al. (2022), the temperature profile of the atmosphere of WASP-39b (which is a hot-Jupiter-type exoplanet) at 10 mbar ranges from 700–1300 K, which is very similar to the physical conditions simulated in this study.

The pressure dependence feature of RMG was enabled to automatically construct pressure-dependent networks for species with up to 10 heavy atoms. Species constraints were set to limit the maximum number of carbon atoms in any molecule to 16 and the maximum number of radicals to three in order to keep the model generation realistic but conserve computing time as well. After the model generation was completed, the final model contained 475 species and 1284 reactions (forward-reverse reaction pairs), which can be found in the supplementary .tar.gz package as well as the RMG input file.

2.3. Rate Coefficients of Photochemical Reactions and Phosphorescence Quenching of $CO(a^3\Pi)$

Since RMG has been developed to simulate the combustion chemistry, it does not include any photochemical reactions in its library. However, it is essential to include photochemical reactions in order to assess the importance of CO photochemistry in the reaction kinetic model. For this reason, we selectively calculated photochemical reaction rate coefficients (k_j) of major species (that were observed in the previous experiments) as a function of the path length (l) and wavelength (λ) under a given experimental total gas pressure (i.e., 15 mbar in Fleury et al. 2019, 2020):

$$k_j(\lambda, l) = \Phi_j(\lambda)\sigma_i(\lambda)F_0(\lambda)e^{-\sum\sigma_i(\lambda)n_i l}, \quad (1)$$

where i represents each gas species (i.e., CO, H_2, H_2O, CH_4, or CO_2), $\Phi_j(\lambda)$ is the quantum yield of the photochemical reaction j, σ_i is the photoabsorption cross sections of the gas species i (see Figure 1(c)), and $F_0(\lambda)$ is a photon flux at the wavelength λ at the photochemical reaction cell window (i.e., $l = 0$ or zero optical depth). Unfortunately, the exact VUV photon flux, $F_0(\lambda)$ profile used in the experiments conducted by Fleury et al. (2019, 2020) was not available. So instead, the $F_0(\lambda)$ profile was taken from Ligterink et al. (2015), which used F-type microwave discharge hydrogen-flow lamps (MDHLs) similar to the system used in the previous experiments and scaled down for input power of 70 W (simulating stellar UV photons) instead of 100 W, and H_2 pressure of 1.2 mbar instead of 0.41 mbar (refer to Figure 4 in Ligterink et al. 2015). The resulting VUV spectra are shown in Figure 1(a). The exponential term is to consider the optical depth caused by the gas species absorbing photons emitted from the UV light source, where n_i is the number density of corresponding gas species i. As shown in Figure 1(b), under the experimental condition of 99.7% H_2 and 0.3% of CO, 15 mbar, and 1473 K, at least more than 40% of Lyα photons are available even at the end of the path length (i.e., l = 48 cm). Equation (1) is then integrated to the photochemical cell length (i.e., $l = 0$ to 48 cm) as shown in Figure 1(d), followed by integration to the wavelength range (i.e., λ = 112–180 nm) to calculate corresponding photochemical reaction rate coefficient (k_j) as listed in Table 1.

A few assumptions have been made with respect to calculating the carbon monoxide photoexcitation (i.e., $X^1\Sigma^+ \rightarrow a^3\Pi$) rate coefficient and phosphorescence (i.e., $a^3\Pi \rightarrow X^1\Sigma^+$;

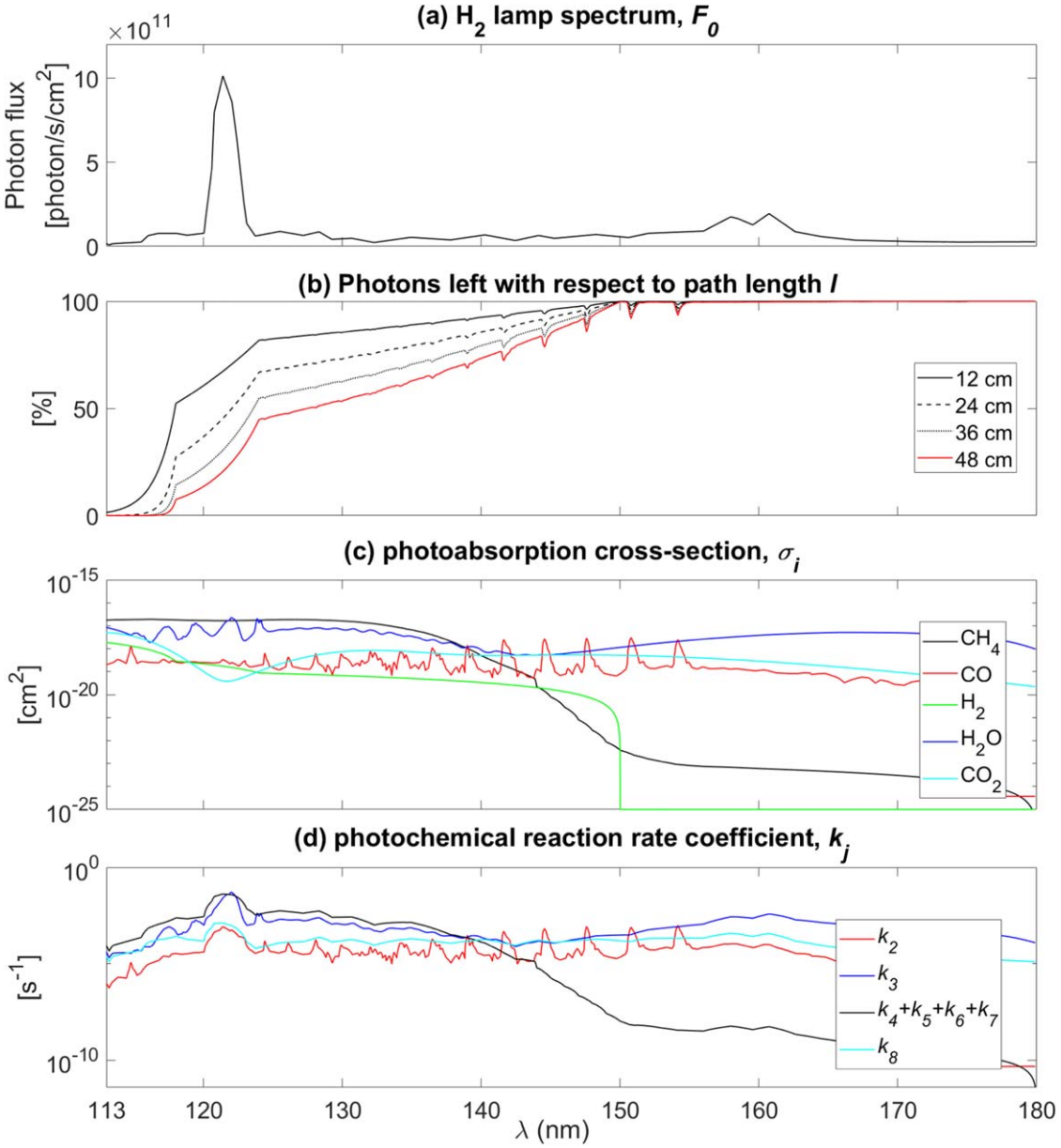

Figure 1. Various parameters necessary to estimate the photochemical reaction rate coefficients of the major species used in this study. Details of how we obtained these parameters shown in this figure are described in Section 2.3. (a) VUV spectra in the 112–180 nm range of F-type MDHL after scaling down the spectral profile taken from Ligterink et al. (2015) for a H_2 pressure of 1.2 mbar, flowing rate of 0.5 sccm, and an input power of 70 W; (b) the proportion of photons of corresponding λ left at 12, 24, 36, and 48 cm of the path length calculated at 1473 K and 15 mbar of total gas pressure of 99.7% H_2 and 0.3% of CO using Equation (1); (c) photoabsorption cross section (σ) profiles of corresponding gas species between 110 and 180 nm. (i) Each σ of CH_4 was taken from Laufer & McNesby (1965) and Mount et al. (1977), (ii) CO was taken from Myer & Samson (1970) and Thompson et al. (1963), (iii) H_2 was taken from Backx et al. (1976), (iv) H_2O was taken from Mota et al. (2005), and (v) CO_2 was taken from Venot et al. (2018); (d) wavelength-dependent rate coefficient $k_j(\lambda)$ of corresponding photochemical reactions defined in Table 1.

note that there is a spin change) rate coefficient, which are (i) every carbon monoxide molecule in the ground state ($X^1\Sigma^+$) populates to $a^3\Pi$ after UV photoexcitation into the spin and dipole allowed $A^1\Sigma$ state; (ii) phosphorescence of CO($a^3\Pi$) down to the ground-state CO($X^1\Sigma^+$) follows an exponential decay pattern determined by the radiative lifetime of the $a^3\Pi$ state; and (iii) there are no significant changes in the radiative rate coefficients for the molecules at different temperatures. In order to implement assumption (i), we assumed the quantum yield (Φ_2) of the CO($a^3\Pi$) after photoexcitation from $X^1\Sigma^+$ to $A^1\Sigma^+$(i.e., $X^1\Sigma^+ \rightarrow a^3\Pi$) to be unity. With regard to assumptions (ii) and (iii), the mean lifetime of CO($a^3\Pi$) was taken from Lee et al. (2020) to be 3 ms.

All these calculated photochemistry-related rate coefficients were later added to the CHEMIKIN format located at the bottom of the CHEMKIN input files indicated as "Newly Added Photochemistry" (see the supplementary .tar.gz package).

2.4. Temperature- and Pressure-dependent Rate Coefficients of H_2 + CO($a^3\Pi$) Reactions

Since the goal of this study is to gain a better insight into simultaneous thermally and photochemically driven reaction pathways involving electronically excited CO in its metastable state ($a^3\Pi$), we need to assess to what extent these metastable

Table 1
Rate Coefficients of Various Photochemistry Included in the Reaction Kinetic Model ($j = 1$ Corresponds to Phosphorescence, $j = 2$ Corresponds to Photoexcitation, and $j = 3$–8 Corresponds to Photodissociation)

j	Reactions	T [K]	k_j [s^{-1}][a]	Notes
1	$CO(a^3\Pi) \rightarrow CO(X^1\Sigma^+)$	…	3.33×10^2	Mean lifetime of 3 ms taken from Lee et al. (2020)
2	$CO(X^1\Sigma^+) \rightarrow CO(a^3\Pi)$	573 873 1173 1473	4.74×10^{-5} 5.18×10^{-5} $5.45(5.19)\times10^{-5}$ $5.64(5.41)\times10^{-5}$	Calculated using Equation (1), Φ_2 of 1 assumed to be unity
3	$H_2O \rightarrow H + OH$	573 873 1173 1473	1.10×10^{-3} 1.20×10^{-3} $1.30(1.20)\times10^{-3}$ $1.40(1.30)\times10^{-3}$	Calculated using Equation (1), Φ_3 of 1 assumed to be unity
4	$CH_4 \rightarrow CH_3 + H$	573 873 1173 1473	5.46×10^{-4} 6.72×10^{-4} $7.14(6.72)\times10^{-4}$ $7.98(7.14)\times10^{-4}$	Calculated using Equation (1), Φ_4 of 0.42 taken from Gans et al. (2011)
5	$CH4 \rightarrow CH_2 + H_2$	573 873 1173 1473	6.24×10^{-4} 7.68×10^{-4} $8.16(7.68)\times10^{-4}$ $9.12(8.16)\times10^{-4}$	Calculated using Equation (1), Φ_5 of 0.48 taken from Gans et al. (2011)
6	$CH4 \rightarrow CH + H_2 + H$	573 873 1173 1473	9.10×10^{-5} 1.12×10^{-4} $1.19(1.12)\times10^{-4}$ $1.33(1.19)\times10^{-4}$	Calculated using Equation (1), Φ_6 of 0.07 taken from Gans et al. (2011)
7	$CH_4 \rightarrow CH_2 + H + H$	573 873 1173 1473	3.90×10^{-5} 4.80×10^{-5} $5.10(4.80)\times10^{-5}$ $5.70(5.10)\times10^{-5}$	Calculated using Equation (1), Φ_7 of 0.03 taken from Gans et al. (2011)
8	$CO_2 \rightarrow CO + O$	573 873 1173 1473	1.11×10^{-4} 1.23×10^{-4} $1.31(1.25)\times10^{-4}$ $1.37(1.32)\times10^{-4}$	Calculated using Equation (1), Φ_8 of 1 taken from Venot et al. (2018)

Note.
[a] Numbers in parentheses refer to calculated photochemical reaction rate coefficients under the experimental condition of Fleury et al. (2020) (i.e., 99.26% of H_2, 0.48% of H_2O, and 0.26% of CO) whose optical depth is slightly larger compared to the experimental condition of Fleury et al. (2019) (i.e., 99.7% of H_2 and 0.3% of CO).

and reactive carbon monoxide molecules (i.e., CO in $a^3\Pi$ state) affect the whole chemistry observed in the experiments by Fleury et al. (2019, 2020). In order to achieve this, it is critical to estimate and include reactions between the most dominant gas species (i.e., H_2) and the excited carbon monoxide in the reaction kinetic modeling. For this reason, we first carried out the potential energy surface (PES) calculations of H_2 + CO previously explored by Euclides & Barreto (2019). The CBS-QB3 method was performed on the stationary points and transition states reported by Euclides & Barreto (2019) using Gaussian 09 (Frisch et al. 2009) and all these molecular parameter outputs are available in the supplementary .tar.gz package. Then as shown in Figure 2, instead of connecting H_2 + $CO(X^1\Sigma^+)$ to the entire PES, we connected H_2 + $CO(a^3\Pi)$ to the entire PES via Transition State 1 (TS1) and TS4 with the assumptions that the entrance barriers of TS1 and TS4 are zero (i.e., barrier-less reactions).

For the next step, after finishing the PES calculation, Arkane (Allen et al. 2012) was used to calculate temperature- and pressure-dependent rate coefficients $k(T,P)$ of the H_2 + $CO(a^3\Pi)$ channels based on the CH_2O PES mentioned above. Briefly, Arkane is a tool that can calculate pressure-dependent phenomenological rate coefficients $k(T,P)$ for unimolecular reaction networks based on the results of quantum chemistry calculations (i.e., PES) and the Rice–Ramsperger–Kassel–Marcus theory (Marcus 1952). Arkane first generates a detailed model of the reaction network using the one-dimensional master equation methods (Miller & Klippenstein 2006) and then applies one of several available model reduction methods (e.g., the modified strong collision approximation) to simplify the detailed model into a set of phenomenological rate coefficients $k(T,P)$ that are suitable for use in chemical reaction mechanisms.

The reservoir state method was used in calculating $k(T,P)$ from the CH_2O pressure-dependent networks. Lennard–Jones parameters of H_2 and CH_2O isomers (approximated to be the same as those for C_2H_6) in helium bath gas were taken from Jasper et al. (2015). The collisional energy-transfer parameters, $\langle \Delta E_{\rm down} \rangle = \alpha_{300} \left(\frac{T}{T_0} \right)^{\rm n}$ $\rm cm^{-1}$, were also taken from Jasper et al. (2015). There are four reaction channels from H_2 + $CO(a^3\Pi)$ and their rate coefficients under the experimental conditions of

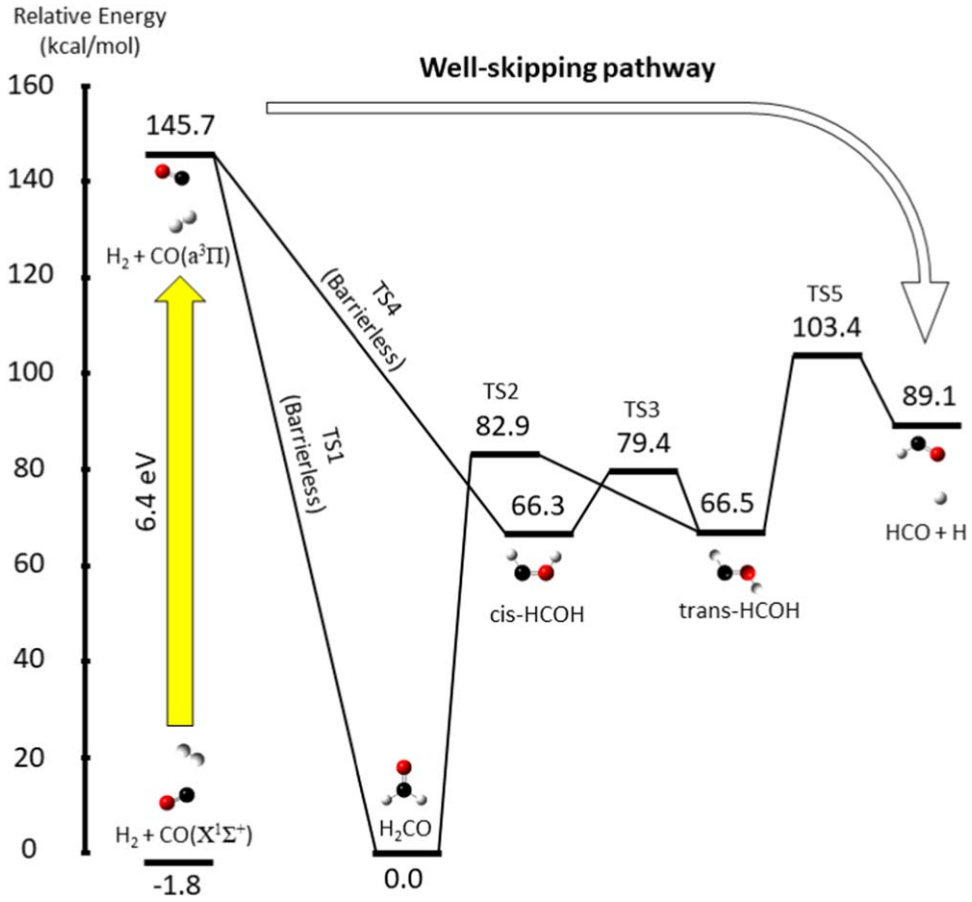

Figure 2. The CH_2O potential energy surface calculated at the CBS-QB3 level of theory. The calculated energy of TS1 and TS4 were originally 81.8 and 104.9 kcal mol^{-1} at the CBS-QB3 level of theory, but here assumed to be barrier-less reactions with respect to $H_2 + CO(a^3\Pi)$. For the definition of *well-skipping pathway*, please refer to Section 3.1.

Table 2
Reaction Rate Coefficients of $H_2 + CO(a^3\Pi)$ and $CO(X^1\Sigma^+) + CO(a^3\Pi)$ Under the Different Temperature Conditions of Fleury et al. (2019, 2020)[a,b,c]

Reactions	573 K	873 K	1173 K	1473 K
$H_2 + CO(a^3\Pi) \rightarrow H + HCO$	$6.83 \times 10^{12}(1.00\times10^{-26})$	$6.44 \times 10^{12}(4.47\times10^{-13})$	$7.32 \times 10^{12}(2.43\times10^{-6})$	$8.94 \times 10^{12}(2.55\times10^{-2})$
$H_2 + CO(a^3\Pi) \rightarrow H_2CO$	$1.82 \times 10^{-15}(1.14\times10^{-19})$	$2.77 \times 10^{-9}(1.25\times10^{-9})$	$6.94 \times 10^{-6}(7.09\times10^{-5})$	$8.21 \times 10^{-4}(3.60 \times 10^{-2})$
$H_2 + CO(a^3\Pi) \rightarrow$ *cis*-HCOH	$8.42 \times 10^{-19}(4.52\times10^{-23})$	$8.78 \times 10^{-13}(3.50\times10^{-13})$	$1.15 \times 10^{-9}(1.13 \times10^{-8})$	$7.26 \times 10^{-8}(3.31\times10^{-6})$
$H_2 + CO(a^3\Pi) \rightarrow$ *trans*-HCOH	$5.65 \times 10^{-19}(3.09\times10^{-23})$	$3.65 \times 10^{-13}(1.49\times10^{-13})$	$3.53 \times 10^{-10}(3.58\times10^{-9})$	$1.93 \times 10^{-8}(9.03\times10^{-7})$
$CO(X^1\Sigma^+) + CO(a^3\Pi) \rightarrow C(^3P) + CO_2$	$2.07 \times 10^{6}(3.44\times10^{-50})$	$2.60 \times 10^{8}(9.19\times10^{-29})$	$3.42 \times 10^{9}(3.34\times10^{-18})$	$1.79 \times 10^{10}(6.88\times10^{-12})$

Notes. The method to estimate the rate coefficients of $H_2 + CO(a^3\Pi)$ is described in detail in Section 2.4, while the individual behavior of each reaction is described in detail in Section 3.1. The rate coefficient of the $CO(X^1\Sigma^+) + CO(a^3\Pi)$ reaction was estimated following the method described in Section 2.5 and its behavior is described in detail in Section 3.2.

[a] Pressure condition is 15 mbar.

[b] Unit is [$cm^3\ mol^{-1}\ s^{-1}$].

[c] Numbers in parentheses refer to calculated rate coefficients of corresponding reactions when CO is in the ground-state ($X^1\Sigma^+$).

Fleury et al. (2019, 2020) are listed in Table 2 as well as the rate coefficients of the reaction of $H_2 + CO(X^1\Sigma^+)$ for a comparison. These reaction coefficients also can be found in CHEMKIN format in the supplementary .tar.gz package. Since the RMG-generated thermochemical reaction model did not distinguish HCOH isomers (*cis*- and *trans*-HCOH), the rate coefficients of $H_2 + CO(a^3\Pi) \rightarrow$ *cis*-HCOH and $H_2 + CO(a^3\Pi) \rightarrow$ *trans*-HCOH were summed up together and appended as the rate coefficient of $H_2 + CO(a^3\Pi) \rightarrow$ HCOH into the CHEMKIN format file (see the supplementary .tar.gz package).

2.5. Temperature-dependent Rate Coefficients of the $CO(X^1\Sigma^+) + CO(a^3\Pi) \rightarrow C(^3P) + CO_2$ Reaction

In the previous study by Fleury et al. (2019), the reaction between the excited CO and the ground-state CO was suggested as the important reaction that might rationalize the formation of CO_2 (along with $C(^3P)$) observed in the experiments. Since carbon monoxide was the second most abundant species in the system, it is important to estimate and include this reaction in the kinetic modeling. Since the potential energy surface of this system was already explored at the CCSD(T)/def2-qZVP level of theory (which is an even higher

level of theory compared to CBS-QB3) with the ωB97M-V/6-311 + G* zero-point correction by DeVine et al. (2022) (shown in Figure 9) with all the required parameters (e.g., potential energy differences, rotational constants, vibrational frequencies, symmetry number, etc.) available, all these parameters were manually provided as an Arkane input rather than carrying out ab initio calculation at the CBS-QB3 level of theory from the beginning. As long as each potential energy is calculated at the same level of theory, the uncertainty of the estimated reaction rate coefficients were good enough for the reaction kinetic modeling purpose. Arkane then generated temperature-dependent rate coefficients using conventional transition state theory (Allen et al. 2012). (Arkane input and output files are available in the supplementary .tar.gz package.) Temperature-dependent rate coefficients of the $CO(X^1\Sigma^+) + CO(a^3\Pi) \rightarrow C(^3P) + CO_2$ reaction at various temperatures are available in Table 2.

2.6. Model Simulation and Analysis

With the reaction mechanism built following the procedure mentioned above, simulations (solving differential equations) were performed for the reaction time of 18 hr (i.e., 64,800 s) on eight experimental conditions of Fleury et al. (2019) (i.e., with UV and without UV at each $T = 573$, 873, 1173, and 1473 K with the initial composition of 99.7% of H_2 and 0.3% of CO) and four experimental conditions of Fleury et al. (2020) (i.e., with UV and without UV at each $T = 1173$ and 1473 K with the initial composition of 99.26% of H_2, 0.26% of CO, and 0.48% of H_2O) using the Reaction Mechanism Simulator (RMS; Johnson et al. 2019), a package included in the RMG (Gao et al. 2016) suite package. The model output is a set of temperature-dependent molecular mixing ratio profiles of each of the species, summarized in Figures 6, 8(a), and 9, which add up to 1 (e.g., a molecular mixing ratio of 10^{-6} in Figure 6 refers to 1 ppm).

Additional model simulations were performed on the same experimental conditions of Fleury et al. (2019) except for higher temperatures (i.e., each $T = 2000$ and 2500 K). The model simulation for a longer reaction time (206 hr), higher pressure (81 mbar), and a temperature of 1473 K was also performed using the RMS. The reactor was assumed as isobaric, isothermal, and homogeneous. Rate of production (ROP) analysis was done using the RMS and the ROP analysis of the kinetic model describing Fleury et al. (2019) is available in Appendix A. Sensitivity analysis was done using the RMG suite package (Gao et al. 2016).

3. Results and Discussion

3.1. $H_2 + CO(a^3\Pi)$ Reaction Rate Coefficients

As shown in Table 2 and Figure 3, the rate coefficient of the $H_2 + CO(a^3\Pi) \rightarrow H + HCO$ reaction is at least 10 orders of magnitude faster than the rate coefficients of any other channels, which indicates that the reaction between UV-excited CO and H_2 will dominantly proceed into H and HCO molecules under any temperature and pressure condition. The $H_2 + CO(a^3\Pi) \rightarrow H + HCO$ reaction is also called the *well-skipping reaction*, which refers to an elementary reaction that traverses more than one transition state dividing surface in a single elementary step (see Figure 2). This well-skipping behavior is mainly attributed to UV-excited CO's excessively high potential energy compared to the potential energy of all the other species and transition states. As shown in Figure 2, the potential energy of (photo)chemically activated reactants (i.e., $H_2 + CO(a^3\Pi)$) is already ∼40 kcal mol^{-1} above the second highest potential energy (i.e., the potential energy of TS4, 104.9 kcal mol^{-1}). For this reason, even under a higher pressure condition of 100 bar, increased collisional stabilization into other stable molecules (i.e., HCOH isomers and H_2CO) is still not efficient enough to beat this well-skipping reaction to form HCO and H. For a similar reason (i.e., excessive energy from UV photons), the UV-excited well-skipping channel is less sensitive to temperature changes compared to other reaction channels. However, this is not the case when CO is in the ground state. As can be seen from Table 2, in the case of the reaction between H_2 and CO in the ground state (i.e., $X^1\Sigma^+$), the reaction channel of $H_2 + CO(X^1\Sigma^+) \rightarrow H_2CO$ remains the main channel up until 1173 K, while the well-skipping reaction (i.e., $H_2 + CO(X^1\Sigma^+) \rightarrow H + HCO$) starts to take over the main channel from the $H_2 + CO(X^1\Sigma^+) \rightarrow H_2CO$ channel at the temperature somewhere above 1473 K (see numbers in parentheses in Table 2). This is because the only energy source for the reactants ($H_2 + CO(X^1\Sigma^+)$) to overcome the reaction barrier of 103.4 kcal mol^{-1} (i.e., TS5 in Figure 2) to form HCO and H is from thermal energy. Up until 873 K, thermal energy is not enough so the intermediates that overcome the reaction barrier of 81.8 kcal mol^{-1} (i.e., TS1) will stabilize into H_2CO rather than skipping all the other wells to form HCO and H. With increasing temperatures above 1173 K, the reactants are more thermally energized so that they are more likely to proceed to the well-skipping channel (i.e., $H_2 + CO(X^1\Sigma^+) \rightarrow H + HCO$) and compete with the stabilization channel down to H_2CO. So the major difference between the $H_2 + CO$ chemistry with and without UV photons would be whether this well-skipping channel (i.e., $H_2 + CO \rightarrow H + HCO$) is dominant (i.e., with UV) or not (i.e., thermal only). These results demonstrate the importance of rigorous reaction kinetics modeling, including photochemical reaction pathways. In the previous study by Fleury et al. (2019), the $CO(X^1\Sigma^+) + CO(a^3\Pi) \rightarrow C(^3P) + CO_2$ reaction was considered the only important photochemistry regardless of dominant H_2 in the system. It was not immediately evident that the reaction $H_2 + CO(a^3\Pi) \rightarrow$ the H + HCO reaction is the most predominant channel and has several orders of magnitude higher rate coefficients than other reaction channels (e.g., $H_2 + CO(a^3\Pi) \rightarrow H_2CO$). This has the important consequence that the H atoms generated are now very reactive and start radical chain reactions.

3.2. $CO(X^1\Sigma^+) + CO(a^3\Pi) \rightarrow C(^3P) + CO_2$ Reaction Reaction Rate Coefficients

As shown in Figure 4, the $CO(X^1\Sigma^+) + CO(a^3\Pi)$ reaction has a nonzero reaction barrier (i.e., 14.24 kcal mol^{-1}) even after the photoexcitation of the ground-state CO, different from $H_2 + CO(a^3\Pi)$ reactions (i.e., barrier-less reactions). For this reason, the calculated reaction rate coefficient shows significant positive temperature dependency as shown in Figure 4. The last row of the Table 2 shows ∼4 orders of magnitude difference between the rate coefficient at the lowest temperature (i.e., 573 K) and the rate coefficient at the highest temperature (i.e., 1473 K). So we can easily predict that this reaction will play a more significant role at elevated temperatures. It is also clear from Table 2 that this reaction would be insignificant without UV photons (even at 1473 K, the rate coefficient is still smaller than 10^{-13} cm^3 mol^{-1} s^{-1}), which makes a major difference between the chemistry with and without UV photons (i.e., thermal only).

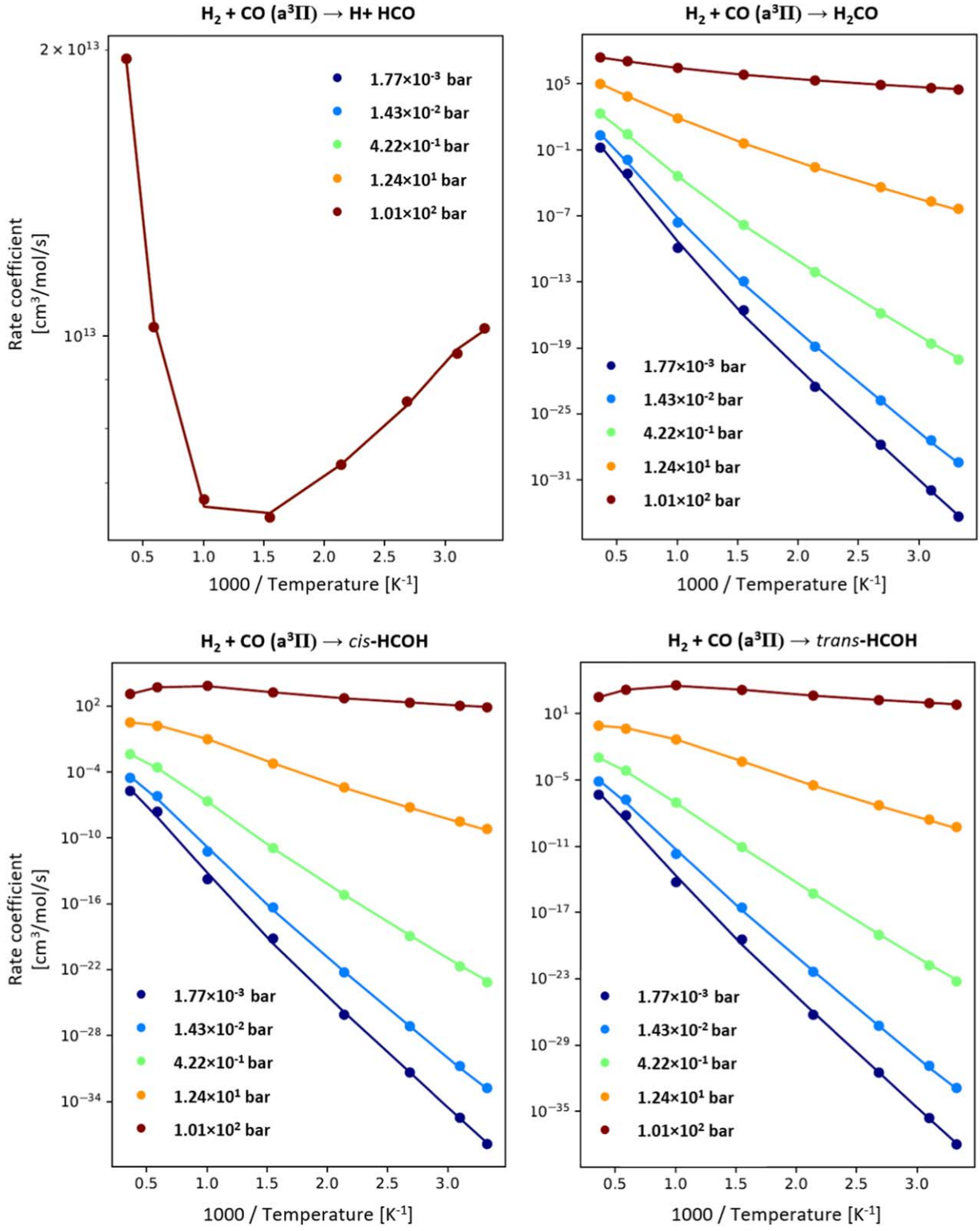

Figure 3. Calculated temperature- and pressure-dependent rate coefficients of the $k(T,P)$ of $H_2 + CO(a^3\Pi)$ channels based on the CH_2O PES in Figure 2. Note that $H_2 + CO(a^3\Pi) \rightarrow H + HCO$ pressure-dependent rate coefficients overlap with each other, thus showing only one plot. The individual behavior of each reaction shown in these plots is described in detail in Section 3.1.

3.3. Modeling of the H_2/CO Exoplanet Atmosphere Analog of Fleury et al. (2019)

3.3.1. Reaction Kinetics of Thermal-only Chemistry

As shown in Figure 6, all major species (i.e., CH_4, H_2O, CO_2, and H radical) formations under thermal-only conditions are predicted to be extremely temperature dependent. This is mainly attributed to elevated reaction rate coefficients with increasing temperature, leading to the formation of major species. This predicted behavior qualitatively matches well with the previous experimental results of Fleury et al. (2019) using the quartz cell. For example, the absorption infrared (IR)

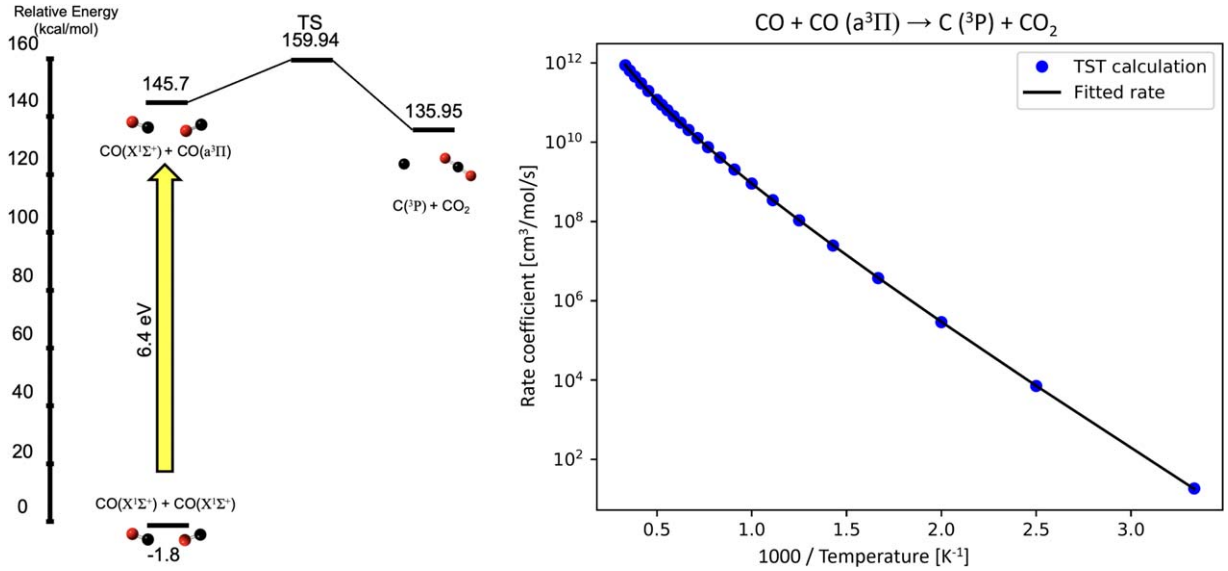

Figure 4. (Left) The triplet C_2O_2 potential energy surface calculated at the CCSD(T)/def2-qZVP level of theory with ωB97M-V/6-311 + G* zero-point correction by DeVine et al. (2022). (Right) Temperature-dependent rate coefficients of the $CO(X^1\Sigma^+) + CO(a^3\Pi) \rightarrow C(^3P) + CO_2$ reaction calculated by Arkane (Allen et al. 2012) using conventional transition state theory.

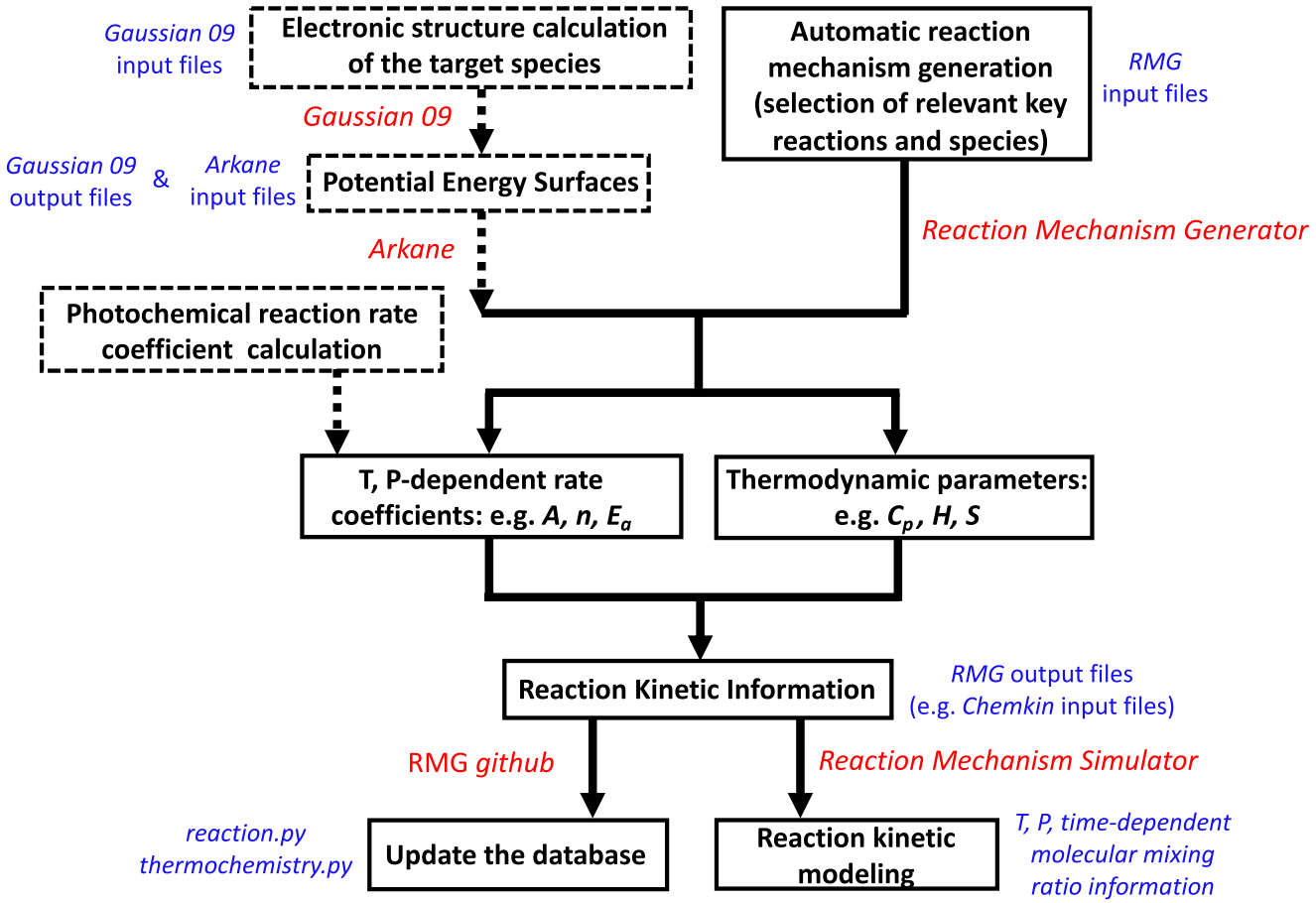

Figure 5. Schematic diagram of the flow of the reaction kinetic modeling carried out in this study. The red-colored text refers to the software tools used in this study. The blue-colored text refers to the inputs and outputs necessary in this study (some of which are mentioned in the main text). The black-colored text in the boxes refers to the major steps described in the main text. For example, *automatic reaction mechanism generation* is described in Sections 2.1 and 2.2, while the *photochemical reaction rate coefficient calculation* shown in this figure is discussed in Section 2.3, and the *potential energy surfaces* are discussed in Section 2.4. The solid line refers to the procedure for generating the thermochemical reaction model. The dashed line refers to the procedure for estimating the photochemical reaction rate coefficients or any rate coefficients that need to be estimated from the first-principle methods (i.e., ab initio calculations) due to various reasons (e.g., there is no available reaction rate coefficient in a previous study).

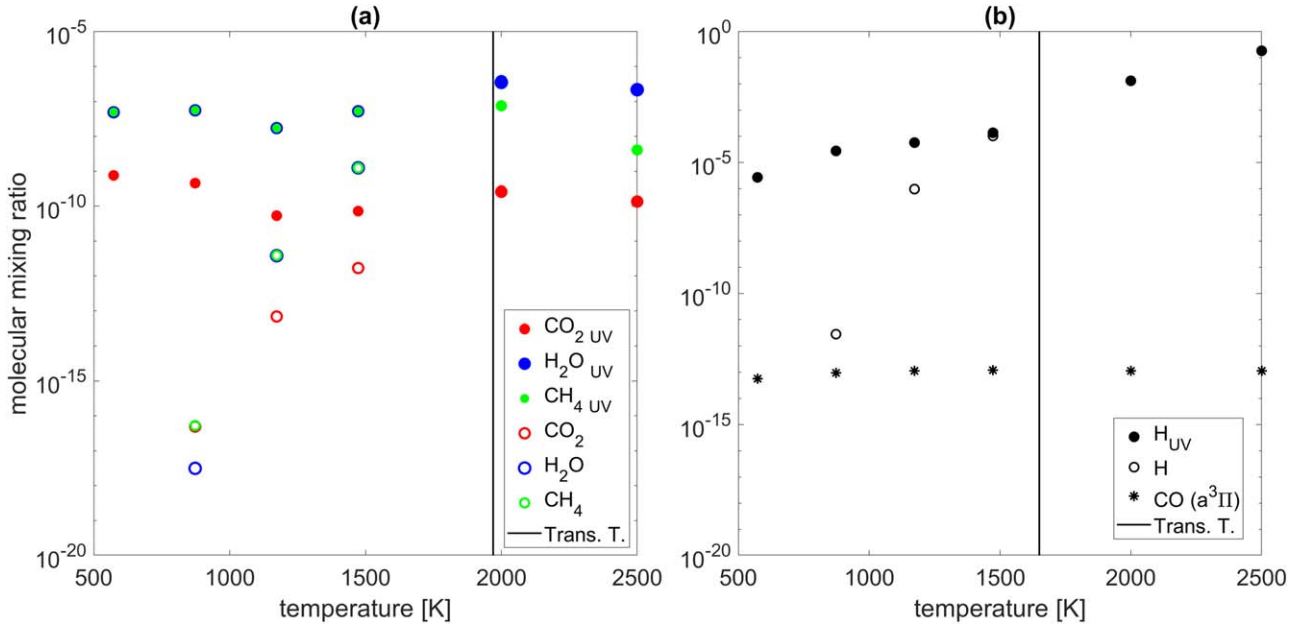

Figure 6. Temperature-dependent molecular mixing ratio profiles predicted by the reaction kinetic modeling for the experimental conditions described in Fleury et al. (2019) and extra simulation up to 2500 K. Solid symbols indicate predicted mixing ratios of molecular species with both thermal energy and UV photons, while open symbols indicate predicted mixing ratios of molecular species under the thermal-only condition (i.e., without UV photons). Please note that several open symbols (i.e., thermal-only chemistry) overlap with solid symbols. The solid lines refer to the transition temperature at which the molecular mixing ratios of each species formed in different systems (i.e., thermal + UV vs. thermal only) only differ by less than 10%): (a) Red circles indicate CO_2; blue circles indicate H_2O; green circles indicate CH_4; the transition temperature with regard to CH_4, H_2O, and CO_2 is calculated to be 1970 K; CO_2, CH_4, and H_2O mixing ratios under the thermal-only condition at 573 K are predicted to be lower than 10^{-20} (i.e., the absolute tolerance of the differential equation solver) and not shown in Figures 6(a) and (b) black circles indicate H atom (radical species); Asterisks indicate UV-excited CO (i.e., carbon monoxide in the $a^3\Pi$ state); the transition temperature with regard to H_2 is calculated to be 1650 K.

spectrum of CO_2 and H_2O show up at 573 K and increase with temperatures. The model predicts that the molecular mixing ratio of these molecules might be too low ($\sim 10^{-28}$ or lower) to be observed experimentally, but it has to be noted that the surface chemistry happening on the wall of the quartz cell might have affected the reaction chemistry. Compared to H_2O and CO_2, CH_4 has much lower absorption cross sections of IR, thus the IR peaks of CH_4 start showing up at 1173 K in the quartz cell used in Fleury et al. (2019). The predicted molecular mixing ratio of CH_4 and H_2O after the reaction time of 18 hr is almost the same. This predicted behavior is due to their formation pathways shown in Figure 7(a). According to the ROP analysis (see Appendix A), the predicted major precursors of CH_4 and H_2O over the entire reaction time (i.e., 18 hr) are CH_3 and OH, respectively. These radical species (i.e., CH_3 and OH) are simultaneously formed through the reaction HCOH + $H_2 \rightarrow CH_3$ + OH under all temperature conditions (additionally formed through the reaction $CH_2OH + H \rightarrow CH_3 + OH$ at temperatures above 1173 K), and respectively, react with H_2 to form their corresponding stable species along with the H atom. Up until 1173 K, HCOH is directly formed through the reaction $H_2 + CO \rightarrow$ HCOH followed by HCOH + $H_2 \rightarrow CH_3$ + OH or the unimolecular reaction (i.e., isomerization) into CH_2O. However, at temperatures above 1173 K, CH_2O starts to isomerize back to HCOH, which eventually leads to the increased formation of CH_4 and H_2O. CH_2O can also be formed through either $H_2 + CO \rightarrow CH_2O$ under all temperature conditions or HCO + $H_2 \rightarrow CH_2O$ + H (only at $T \geqslant 873$ K). HCO forms through H_2 + CO → H + HCO, but readily dissociates back to CO + H. However, as mentioned previously, at $T \geqslant 873$, HCO can proceed to CH_2O by reacting with H_2 and at $T \geqslant 1473$ K, HCO can be produced through the additional reaction H + CO → HCO.

H radicals are formed in a significant amount at $T \geqslant 873$ K through thermal dissociation into H radicals (i.e., $H_2 \rightarrow 2H$), while the recombination back to H_2 (i.e., H + H → H_2) becomes significant at $T \geqslant 1473$ K after enough H radicals are formed in the system. CO_2 is formed through CO + OH → H + CO_2 at T ⩽ 1173 K. But at $T \geqslant 1473$ K, CO_2 is formed through $CH_2O + CO \rightarrow CH_2 + CO_2$, while CO_2 reacts with H radical and forms CO and OH (not indicated in Figure 7(a)). This reaction (i.e., $CO_2 + H \rightarrow CO + OH$) is attributed to an increased amount of H radicals due to elevated thermal dissociation of H_2 at elevated temperatures. Overall, as can be seen in Figure 7(a), with increasing temperatures, additional reaction pathways are being added to the system and push the chemistry to the right side of the figure toward the formation of CH_4, H_2O, and CO_2.

It is also interesting to observe that the model predictions of molecular mixing ratios of species under thermal-only conditions become similar to those under the condition with UV photons at around 2000 K. At $T = 1970$ K, the amount of CH_4, H_2O, and CO_2 formed in the system with UV photons was only different by less than 10% compared to that under the thermal-only system. In this paper, we call this temperature a *transition temperature* with regard to these species (i.e., CH_4, H_2O, and CO_2). This indicates that at temperatures higher than 2000 K, thermally driven reactions are fast enough that the system becomes less sensitive to UV photons compared to the system at lower temperatures. This feature has already been suggested

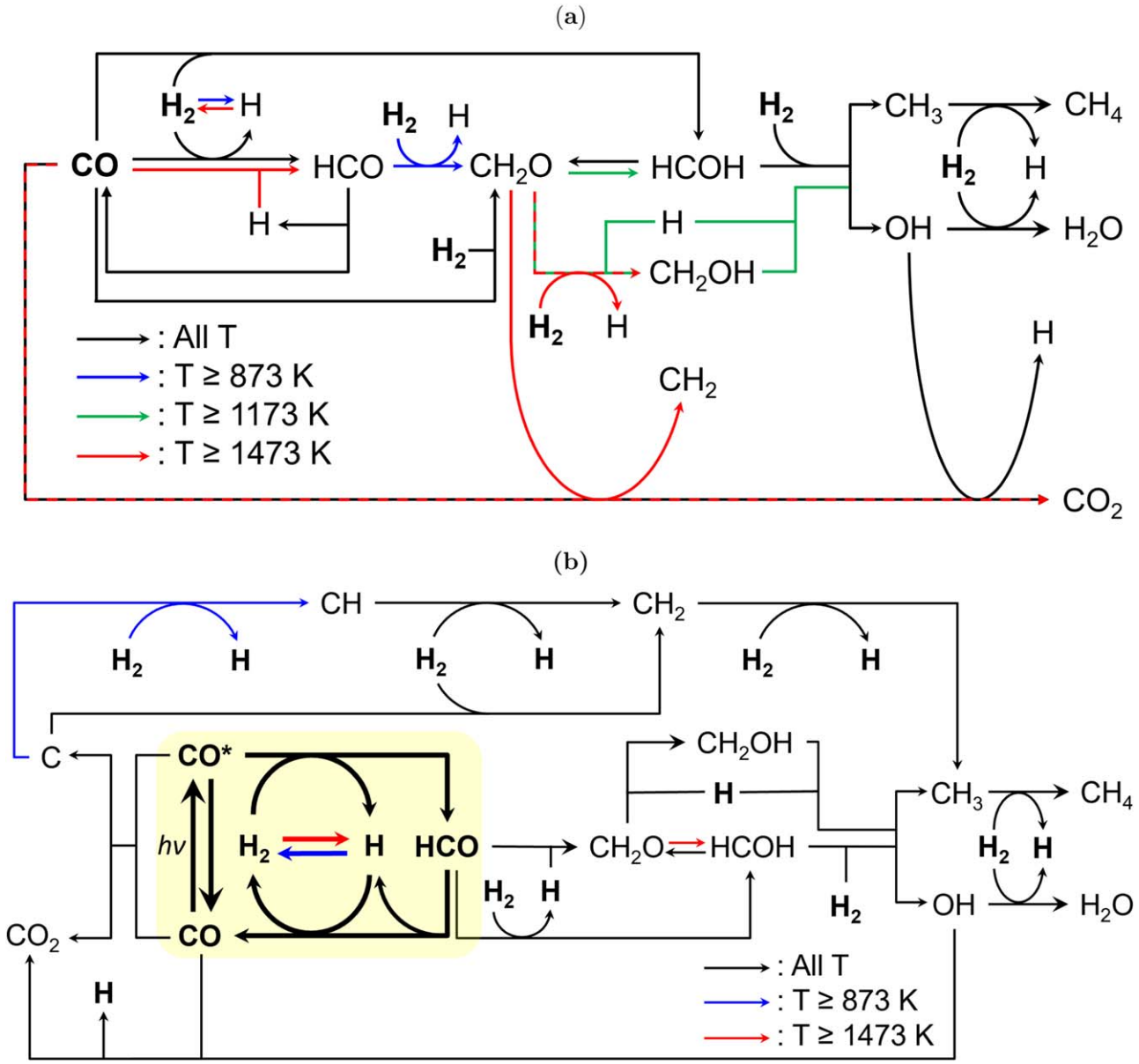

Figure 7. Model-predicted major reaction pathways based on the ROP analysis describing previous experimental studies of Fleury et al. (2019, 2020) under various temperature conditions indicated by the color of the lines: (a) without UV photons, and (b) with UV photons. Reaction rates inside the yellow highlighted region in panel (b) are at least around three orders of magnitude faster than the rates of any other reactions in the model.

in previous theoretical studies (Moses et al. 2011; Venot et al. 2012; Moses 2014). However, it has to be noted that there are multiple factors (e.g., other photochemical reactions not considered in this study, temperature-dependent UV-photo-absorption cross sections of carbon monoxide, etc.) that can change the transition temperature and this will be discussed later. Also, it is predicted from the model that the molecular mixing ratios of all major species (i.e., CH_4, H_2O, and CO_2) decrease at the temperature above this transition temperature, which means that all these major species have reached quasi-equilibrium and are not favored under this temperature condition anymore. In the case of CH_4, the decrease in molecular mixing ratio at temperatures higher than 2000 K is more significant compared to molecular mixing ratios of H_2O and CO_2. This behavior is due to the thermal conversion of CH_4 into C_2 species (mainly C_2H_2). This will be discussed in detail in a later section.

3.3.2. Reaction Kinetics of Thermal and UV Photochemistry

The most notable feature shown from the reaction kinetic modeling of simultaneous thermal and UV photochemistry is the significant increase of the molecular mixing ratios of all the species at all temperatures compared to the case with thermal-only chemistry (see Figure 6). All the species (i.e., CH_4, H_2O, CO_2, and H radicals) are predicted to be produced at least ~20 orders of magnitude, ~7 orders of magnitude, and ~3 orders of magnitude more under the thermal and UV photochemistry condition than under the thermal-only condition at temperatures of 573, 873, and 1173 K, respectively. At a temperature of 1473 K, all these species are predicted to be formed ~40 times more under the thermal and UV photochemistry condition compared to the predicted productions of the species under the thermal-only condition. Figure 6(b) shows that the molecular mixing ratio of $CO(a^3\Pi)$ is not sensitive to temperature difference, which indicates that only the photochemical cycle

(mentioned later) determines its abundance in the system. Overall, the model prediction can well explain significantly augmented formations of CH_4, H_2O, and CO_2 under all temperature conditions ($T \leqslant 1473$ K) under simultaneous thermal and UV photochemistry, as shown in Figure 6 of Fleury et al. (2019).

If we look at the major reaction pathways based on the ROP analysis as shown in Figure 7(b), we can see that the chemistry of the whole system under all temperature conditions is dominated by one photochemical cycle indicated in the yellow highlighted region: (i) carbon monoxide in the ground state gets electronically excited to the $a^3\Pi$ state by UV photons, (ii) excited CO can either go down to the ground-state CO within its radiative lifetime of 3 ms (Lee et al. 2020) or react with H_2 to form H and HCO, and (iii) HCO can either dissociate into H + CO or react with H radical to disproportionate to H_2 and CO. At elevated temperatures, H radical recombination (i.e., H + H $\rightarrow$ H_2 at $T \geqslant 873$ K) and H_2 dissociation ($H_2 \rightarrow H + H$ at $T \geqslant 1473$ K) also become dominant as well. Based on the ROP analysis, these major reaction pathways of the highlighted cycle are at least $\sim$3 orders of magnitude faster than any other reactions shown (or not shown if they are minor reactions) in Figure 7(b). For this reason, a significant amount of HCO becomes available with the aid of this photochemical cycle even at very low temperatures such as 573 K, which makes the chemistry of the system very different from thermal-only chemistry. As a result, every chemical reaction that is involved with HCO becomes much more efficient with UV photons than it used to be in thermal-only chemistry, which in turn pushes the whole chemistry to the right side of Figure 7(b) and eventually leads to the augmented formation of CH_4, H_2O, and CO_2, in agreement with the experimental observations of Fleury et al. (2019).

The reaction between the photoexcited CO and the ground-state CO that forms a triplet C atom and CO_2 turns out to be very important according to the kinetic model, especially at high temperatures above 873 K. As shown in Figure 7(b), this reaction efficiently forms CO_2 and the triplet C atom first. The C atom will then be hydrogenated by reacting with H_2 into CH, CH_2, and then CH_3 step by step, which will form CH_4. Along with every hydrogenation step (i.e., $CH_n + H_2 \rightarrow CH_{n+1} + H$), H radicals are efficiently formed and then attack CO_2 to form OH radicals as well, which will form H_2O. As mentioned earlier in Section 3.2, due to its temperature dependency of the $CO(X^1\Sigma^+) + CO(a^3\Pi) \rightarrow C(^3P) + CO_2$ reaction, this reaction will be more important at elevated temperatures. According to our kinetic model result, significantly augmented formations of major species (CH_4, H_2O, and CO_2) are attributed to the $H_2 + CO(a^3\Pi) \rightarrow H + HCO$ reaction up until 873 K, while the augmented major species formations are attributed to the $CO(X^1\Sigma^+) + CO(a^3\Pi) \rightarrow C(^3P) + CO_2$ reaction at temperatures above 873 K. In short, two different photochemical schemes (i.e., $H_2 + CO(a^3\Pi) \rightarrow H + HCO$ versus $CO(X^1\Sigma^+) + CO(a^3\Pi) \rightarrow C(^3P) + CO_2$) determine the mixing ratios of CH_4, H_2O, and CO_2 at different temperature regions below the transition temperature (i.e., 1970 K for CH_4, H_2O, and CO_2), respectively. With regard to H radicals, however, it has to be noted that $H_2 + CO(a^3\Pi)$ mainly determines the mixing ratio of H radicals in the system at temperatures below the transition temperature (i.e., 1650 K for H radicals).

In contrast to thermal-only chemistry, the molecular mixing ratio of CH_4, H_2O, and CO_2 wiggles as shown in Figure 6(a). These molecules have been efficiently formed as a result of UV photochemistry enhanced by metastable $a^3\Pi$ state carbon monoxide and remain relatively stable at relatively lower temperatures below 873 K (i.e., UV photochemistry determines their mixing ratio after the reaction time of 18 hr). However, at 1173 K, thermal chemistry starts to partially determine their mixing ratio and this is well shown at 2000 K in Figure 6(a) where the molecular mixing ratios of CH_4, H_2O, and CO_2 formed with UV photons are not distinguishable from those formed without UV photons (i.e., thermal only). We further simulated the molecular mixing ratio of CH_4, H_2O, and CO_2 at 2000 and 2500 K after 18 hr while maintaining other conditions the same as that at 1473 K, and as expected, there was no significant difference in the molecular mixing ratio of CH_4, H_2O, and CO_2 formed no matter whether UV photons were available or not (see Figure 6). So based on the model prediction (and as mentioned earlier in the text), we can say that the transition temperature where thermal chemistry becomes dominant compared to photochemistry starts at around 1970 K and it has to be noted that this transition temperature can be shifted due to multiple factors including (i) errors in the UV photon fluxes, (ii) errors in photoabsorption cross sections (e.g., temperature dependent) of species, (iii) errors in quantum yields of any photochemical reactions, (iv) any missing reaction species or reactions in the system, (v) any errors in included thermal reactions, and (vi) any errors in included thermodynamic parameters of related species. With regard to this, the sensitivity of the model will be discussed later.

3.3.3. Potential Importance of the Acetylene (C_2H_2) Formation with Regard to the Organic Refractory Aerosol Formation in Hot-Jupiter Exoplanet Atmospheres

Although a detectable amount of solid-phase product was not observed from any of the experiments at the temperature below 1473 K conducted by Fleury et al. (2019) (i.e., 15 mbar; 573–1473 K; with and without UV; reaction time of 18 hr), an observable amount of condensed-phase organic aerosol products as a thin film deposited on sapphire windows was reported by Fleury et al. (2019) after 204 hr of experiments with increased starting total gas pressure of 81 mbar with UV irradiation at 1473 K. Since there was no any direct information about the molecular structure of this aerosol, it is hard to exclusively say whether this observed organic aerosol is composed of aromatic hydrocarbons (if not polycyclic) or not. However, it is logical to say that C_1 species should first go through C_2 species before growing into aerosol particles, which gives us a rationale to look into any C_2 or larger species predicted to be formed during our model simulation. The model simulation of the corresponding experimental condition (i.e., 81 mbar, 1473 K, with UV photons, and the reaction time of 206 hr) predicted the molecular mixing ratio of each species as follows: $[C_2H_6] = 6.62 \times 10^{-15}$, $[C_2H_4] = 7.32 \times 10^{-12}$, and $[C_2H_2] = 1.95 \times 10^{-10}$. Any species larger than C_2 species (e.g., C_3H_3 or larger) were predicted to be around or less than 1.00×10^{-20} (the absolute tolerance of the differential equation solver), which indicates that no significant amount of the species larger than C_2 species are predicted to be formed in the simulated systems even at the temperature of 2500 K.

Among these C_2 species, we focused on the formation of acetylene in the model for the following reason: (i) previous studies have suggested benzene (1-ring aromatic hydrocarbon)

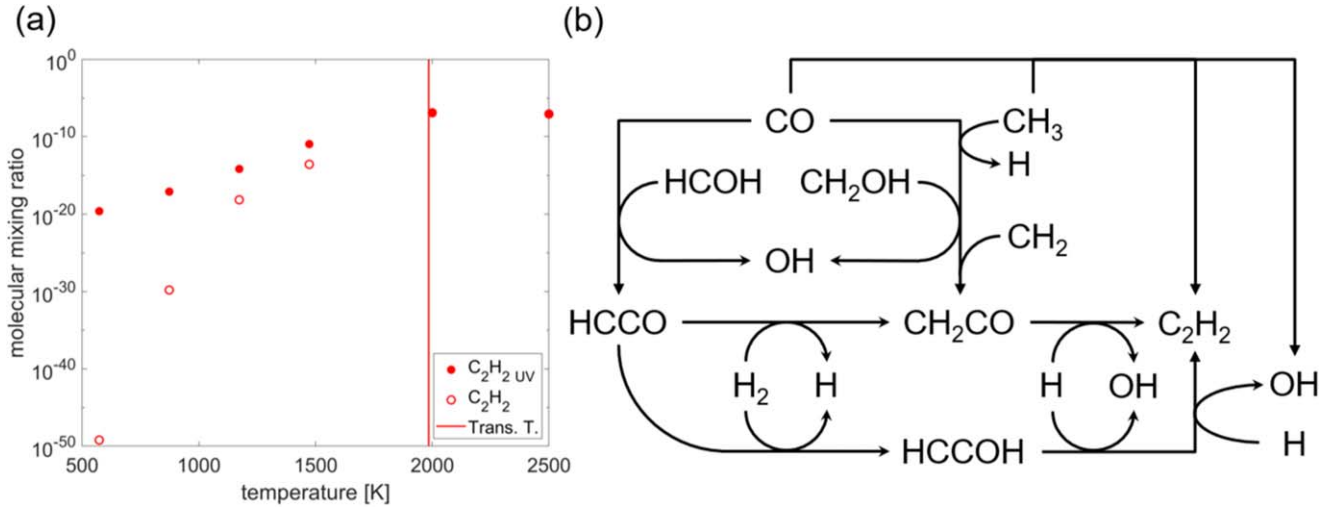

Figure 8. (a) Temperature-dependent mixing ratio profiles of acetylene (C_2H_2) predicted by the reaction kinetic modeling for the experimental conditions described in Fleury et al. (2019). Solid symbols indicate the predicted C_2H_2 mixing ratio with UV photons, while open symbols indicate the predicted C_2H_2 mixing ratio under the thermal-only condition (i.e., without UV photons). The solid line refers to the transition temperature at which the molecular mixing ratio of C_2H_2 formed in different systems (i.e., thermal + UV vs. thermal only) only differs by less than 10%). The transition temperature with regard to C_2H_2 is 1985 K; (b) a schematic diagram of reaction pathways toward C_2H_2 formation based on the ROP analysis

and naphthalene (2-ring aromatic hydrocarbon) as precursors to refractory hydrocarbon aerosols (Trainer et al. 2013; Brem et al. 2015), (ii) one of the prevailing mechanisms that rationalize the formation up to 2-ringed aromatics (including benzene and naphthalene) is the hydrogen-abstraction-acetylene-addition mechanism (HACA), an aromatic radical formed via hydrogen abstraction adds to acetylene (C_2H_2) to form a larger vinylic radical adduct (Bittner & Howard 1981; Frenklach et al. 1985; Parker et al. 2014; Yang et al. 2016; Chu et al. 2019; Smith et al. 2020), and (iii) a previous photochemical experiment by Franklin (2018) using a D_2 lamp (115–170 nm) at 25°C under oxygen-free conditions has shown that the VUV irradiation on C_2H_2 is the most efficient in the formation of organic particles compared to the VUV irradiation on other C_2 species (i.e., C_2H_6 and C_2H_4). Although it is not clear how the formation of acetylene is exactly related to the formation of organic aerosols observed by Fleury et al. (2019), as mentioned earlier, many previous studies indicate a positive relationship between the formation of acetylene and the formation of aerosol.

With this background, if we look at the temperature-dependent mixing ratio profiles of acetylene predicted by the reaction kinetic modeling for the experimental conditions described in Fleury et al. (2019), we can see that UV-excited metastable carbon monoxides can significantly enhance the formation of acetylene compared to thermal-only chemistry as shown in Figure 8(a) at the temperature up to 1473 K. Up until 1173 K, acetylene (C_2H_2) is predicted to be produced at least ~4 orders of magnitude more under the thermal and UV photochemistry condition than under the thermal-only condition as shown in Figure 8(a). At the temperature of 1473 K, acetylene is predicted to be formed ~410 times more under the thermal and UV photochemistry condition compared to the predicted acetylene production under the thermal-only condition. At the temperature above 2000 K, there was no significant difference in the predicted molecular mixing ratio of C_2H_2 formed no matter whether UV photons were available or not, which indicates that the transition temperature is around 2000 K (precisely 1985 K). Figure 8(b) shows major reaction pathways from C_1 species to C_2H_2. As can be seen from Figures A1–A4 in Appendix A, at early timescales (i.e., up to ~10 ms), $CH_3 + CO \rightarrow C_2H_2 + OH$ is the major pathway, and then the major C_2H_2 formation pathway changes to others such as $HCCOH + H \rightarrow C_2H_2 + OH$ or $CH_2CO + H \rightarrow C_2H_2 + OH$. With UV photons available in the system, the UV-elevated amount of HCO results in the elevated formation of HCOH and CH_2OH, which then results in the elevated formation of C_2H_2. However, at temperatures higher than the transition temperature (i.e., 1985 K), thermal chemistry now determines the C_2H_2 mixing ratio as it did with the molecular mixing ratios of CH_4, H_2O, and CO_2. Like the calculated rate coefficient of the reaction between the excited CO and H_2 forming HCO and H is much faster than the rate coefficient of the reaction between the ground-state CO and H_2 forming HCO and H, the rate coefficient of the reaction between the excited CO and CH_3 forming C_2H_2 and OH might affect the formation of C_2H_2 in a significant way. To test this, we recalculated the potential energy surfaces of C_2H_2 + OH taken from Miller & Melius (1989) at the CBS-QB3 level of theory using Gaussian 09 (Frisch et al. 2009) and calculated the temperature- and pressure-dependent rate coefficients of $CH_3 + CO(a^3\Pi)$ reactions following a method similar to that described in Section 2.4 (rate coefficients and the corresponding PES are available in the supplementary .tar.gz package). However, no matter whether $CH_3 + CO(a^3\Pi)$ chemistry is included in the reaction kinetic model or not, no significant change was observed in the formation of C_2H_2. This might indicate that the molecular mixing ratio of CH_3 is still too low to draw any significant increases in the formation of acetylene through $CH_3 + CO(a^3\Pi)$ chemistry.

Table 3 shows the model (thermal and UV photochemistry incorporated) predicted C_2H_2 mixing ratios under different conditions (starting from H_2:CO = 99.7:0.3). As can be seen in Table 3, the model simulation indicates that the formation of acetylene (C_2H_2) is favored with increasing temperature. The model also shows that C_2H_2 formation has not reached a quasi-equilibrium state even after 206 hr (81 mbar) and 18 hr (15 mbar) at 1473 K, respectively (see Figure B1(a), (b) in

Table 3
Comparison of Model-predicted C_2H_2 Mixing Ratios among Various Conditions (Initial Molecular Compositions of H_2:CO = 99.7:0.3) with UV Photons Available[a]

	1473 K, 15 mbar[b] (18 hr)	1473 K, 81 mbar (18 hr)	1473 K, 81 mbar[b,c] (206 hr)	2000 K, 15 mbar (18 hr)	2500 K, 15 mbar (18 hr)
[C_2H_2]	1.10×10^{-11} (2.68×10^{-14})	1.57×10^{-12} (2.18×10^{-13})	1.95×10^{-10} (2.43×10^{-11})	1.37×10^{-7} (1.25×10^{-7})	8.55×10^{-8} (8.55×10^{-8})

Notes.
[a] Numbers in parentheses refer to the calculated molecular mixing ratio of C_2H_2 under the thermal-only condition.
[b] Experimental conditions conducted by Fleury et al. (2019).
[c] Experimental condition from which a detectable amount of solid-phase product was observed in Fleury et al. (2019).

Appendix B). However, at 2000 K, the formation of acetylene reaches its quasi-equilibrium state after 18 hr with its molecular mixing ratio of $\sim 1.37 \times 10^{-7}$ (see Figure B1(c) in Appendix B), and no significant amount of any species larger than C_3 molecules was predicted in the given system. This mainly indicates that (i) the amount of acetylene formed via thermal-only chemistry (up to 2500 K) under the condition of H_2:CO = 99.7:0.3 is not enough to push the chemistry to larger species such as polycyclic aromatic hydrocarbons (PAHs) that are accepted as precursors to organic aerosols in the majority of combustion research (Frenklach & Mebel 2020) and (ii) some major photochemical reactions can bring the chemistry into disequilibrium chemistry to form larger hydrocarbon species (e.g., 1-ring aromatic hydrocarbons or PAHs) or even organic aerosols. With regard to (ii), the results of previous experimental studies (Franklin 2018; Fleury et al. 2019) in combination with the current study in this paper might indicate that the reaction kinetic model including the C_2H_2 photochemistry is the key to explaining the experimentally observed organic aerosol formations from Fleury et al. (2019). Note that our reaction kinetic model including CO($a^3\Pi$) photochemistry was successful in qualitatively explaining the significantly augmented formation of major species (i.e., CH_4, H_2O, and CO_2) observed in Fleury et al. (2019) under all temperature conditions. As can be seen from Table 3, our thermal and UV photochemistry model predicts ~3 orders of magnitude more C_2H_2 are formed in the system under the 2000 K and 15 mbar condition even with an order of magnitude shorter timescale (i.e., 18 hr) compared to the 1473 K and 81 mbar condition with the reaction time of 206 hr. Thus, if our hypothesis (i.e., the amount of C_2H_2 is closely related to aerosol formations) is correct, we are able to observe aerosol formations even at temperatures lower than 2000 K within the reaction time shorter than 18 hr from the same experimental device of Fleury et al. (2019). Conducting this experiment and including C_2H_2-related photochemistry in our current model would be interesting for future studies.

3.3.4. Analysis of the Sensitivity of the Kinetic Model

One of the major features of this study is the assessment of the transition temperature in which thermal chemistry starts to become dominant compared to photochemistry. However, this transition temperature can be affected by multiple factors as mentioned earlier: (i) errors in the UV light sources, (ii) errors in photoabsorption cross sections, (iii) errors in quantum yields of any photochemical reactions, (iv) any missing reaction species or reactions (even surface chemistry), (v) any errors in thermochemical reactions included in the model, and (vi) any errors in thermodynamic parameters of related species. Although (iv) is important when it comes to model improvements, this is beyond the scope of the current work. With regard to (i)–(iii), these three factors directly affect the calculated carbon monoxide photoexcitation rate coefficient (i.e., $X^1\Sigma^+ \rightarrow a^3\Pi$) discussed in Section 2.3. With regard to (v) and (vi), these errors originally came from the embedded errors of rate coefficients imported from the references described in Section 2.1. We computed the sensitivity of the major species (i.e., CH_4, H_2O, and CO_2) to all of the rate coefficients in the model simulated under the condition of 1473 K, 15 mbar, [H_2] = 0.997, and [CO] = 0.003, and the most sensitive three parameters that affect the predicted formation of the major species turn out to be the photochemical reactions

$$CO(X^1\Sigma^+) \rightarrow CO(a^3\Pi), \quad (2)$$

$$CO(X^1\Sigma^+) + CO(a^3\Pi) \rightarrow CO_2 + C(^3P). \quad (3)$$

$$H_2 + CO(a^3\Pi) + M \rightarrow H + HCO + M. \quad (4)$$

They each have normalized sensitivities $\frac{d(lnC_n)}{d(k_i)}$ with magnitudes of around 1, 0.95, and −0.75, respectively (see Figure C1). This means that, for example, if one increases the rate coefficient of reaction (2) by a factor of 10, the predicted molecular mixing ratio of the major species (i.e., CH_4, H_2O, and CO_2) would be increased by 10 times and the transition temperature would be pushed to a much higher temperature. On the contrary, if one reduces this carbon monoxide photoexcitation rate coefficient (i.e., reaction (2), k_2) by a factor of 2, the predicted molecular mixing ratio of the major species (i.e., CH_4, H_2O, and CO_2) would be decreased by ~50% and the transition temperature would be shifted to a lower temperature. The former case is possible if the photoabsorption cross sections of carbon monoxide are underestimated. It has to be noted that the photoabsorption cross sections of CO used to calculate k_2 were taken from Myer & Samson (1970), who experimentally measured the VUV absorption cross sections at 298 K. Since VUV absorption cross sections usually increase with increasing temperatures due to thermally increased populations at higher vibrational states, which then might result in increased access to upper electronic states. Venot et al. (2018) experimentally showed that the photoabsorption cross sections of CO_2 around Lyα can vary by 2 orders of magnitude between 150 and 800 K. For this reason, it might be the case if the photoabsorption cross sections of CO around Lyα increase by more than an order of magnitude from 298–1473 K, which can potentially increase the carbon monoxide photoexcitation rate coefficient (i.e., k_2) by a factor of 10, which means the

calculated k_2 is 10 times underestimated. However, the latter case (i.e., reducing k_2 by a factor of 2) is also possible. It has to be noted that the quantum yield (i.e., Φ_2) used in the calculation of k_2 in Section 2.3 is assumed to be unity since we could not find any theoretically or experimentally determined quantum yield of this photoexcitation reaction. However, it would not be surprising if Φ_2 is 0.5. In this case, the model-predicted molecular mixing ratio would be overestimated by∼50%. These cases suggest interesting future studies (i.e., a measurement of temperature-dependent VUV photoabsorption cross sections of carbon monoxide or a determination of the Φ_2).

It has to be noted that there are too many model parameters and too few experimental data (e.g., a measurement of the CO absorption cross section at various temperatures or a measurement of Φ_2) to allow a perfect determination of the model parameters (and keep in mind that there are several other moderately sensitive rate coefficients and thermochemistry in the model, not just these three most sensitive reactions). However, even considering these, our kinetic modeling work indicates that electronically excited CO in its metastable state ($a^3\Pi$) can push the whole chemistry to the augmented formation of CH_4, CO_2, and H_2O in an obvious way, which qualitatively matches well with the experimental observation from Fleury et al. (2019). The quantitative discrepancy does not indicate a fundamental issue with the reaction kinetic model, but rather reflects our imperfect knowledge of the values of the model parameters.

3.4. Modeling of the H_2/CO/H_2O Exoplanet Atmosphere Analog of Fleury et al. (2020)

When H_2O is added to the H_2/CO mix to change the C/O ratio to more realistic solar elemental abundance, both the kinetic model-predicted thermal-only and UV-incorporated thermal chemistry of Fleury et al. (2020) were almost similar to those of Fleury et al. (2019). The major reaction pathway forming CH_4 (note that H_2O was included from the beginning of the experiments at a much higher mixing ratio, so is not focused on as a product) in Fleury et al. (2020) is predicted to be almost similar to those described in Figure 7 and the previous section of describing the modeling result of Fleury et al. (2019). The major reaction pathways forming CO_2 were exclusively CO being oxidized by OH radicals forming CO_2 and H radicals. This behavior is due to a huge amount of H_2O included in the system from the beginning, which then can either thermally or photochemically dissociate into H and OH radicals in the system. Although the H_2O formation is predicted from our model simulation of Fleury et al. (2019), the amount of the H_2O predicted in the simulation of Fleury et al. (2019) is still way smaller than the amount of H_2O introduced into the system from the beginning of the simulation of Fleury et al. (2020). For this reason, the simulated system of Fleury et al. (2020) would contain much more OH radicals compared to the simulated system of Fleury et al. (2019). This leads to the notable difference between the model simulation of Fleury et al. (2020) and that of Fleury et al. (2019) in the form of the reversed molecular mixing ratio of CH_4 to CO_2. As shown in Figure 9, the molecular mixing ratio of CO_2 is ∼3 orders and ∼4 orders of magnitude larger compared to that of CH_4 at 1173 and 1473 K, respectively. In the case of Fleury et al. (2019), the molecular mixing ratio of CH_4 is always at least

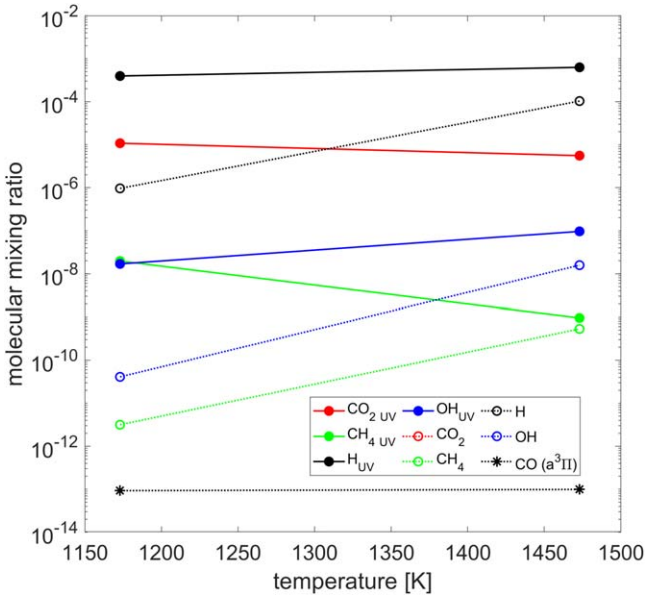

Figure 9. Temperature-dependent molecular mixing ratio profiles predicted by the reaction kinetic model for the experimental conditions described in Fleury et al. (2020). Solid symbols indicate the predicted mixing ratio of molecular species with both thermal energy and UV photons, while open symbols indicate the predicted mixing ratio of molecular species under the thermal-only condition (i.e., without UV photons): (a) red circles indicate CO_2. Predicted CO_2 mixing ratio under the thermal-only condition overlaps with the mixing ratio of CO_2 with UV photons, thus not shown in the figure; blue circles indicate OH; green circles indicate CH_4; black circles indicate H atom (radical species); asterisks indicate UV-excited CO (i.e., carbon monoxide in the $a^3\Pi$ state).

2 orders of magnitude higher than that of CO_2 at temperatures higher than 1173 K, no matter whether UV photons are available or not. As mentioned above, this reversed ratio is attributed to the inclusion of H_2O from the beginning of the kinetic simulation of Fleury et al. (2020). According to the kinetic modeling, H_2O already thermally dissociates to form both H and OH radicals at 1173 K. These OH radicals reach the quasi-equilibrium state within ∼11 hr when the energy source is thermal only, while they reach quasi-equilibrium much faster within 200 s with the aid of UV photons (i.e., photodissociation of H_2O into H + OH). This tendency gets more severe at higher temperature (i.e., 1473 K) in which thermal dissociation becomes much more efficient (since the thermal dissociation rate coefficient is positively temperature dependent). This can be observed in the form of an increasing OH mixing ratio in Figure 9. Compared to 1173 K, the experimental condition of Fleury et al. (2020) is much more oxidizing, so the predicted CH_4 mixing ratio decreases rapidly by 20 times (i.e., from $[CH_4] = 1.97\times10^{-8}$ at 1173 K to $[CH_4] = 9.55\times10^{-10}$ at 1473 K). It also has to be noted that the CO_2 mixing ratio does not show any difference in whether UV irradiation is available or not (see red symbols and lines in Figure 9). This feature indicates that the CO_2 formation has already reached its thermal quasi-equilibrium after 18 hr. As shown in Figure D1 in Appendix D, the CO_2 mixing ratio at 1173 K reaches equilibrium within 7 hr under the thermal-only condition, and 50 s with UV irradiation, while the CO_2 mixing ratio at 1473 K reaches equilibrium within 200 s under the thermal-only condition, and 30 s with UV irradiation. According to our model prediction, the predicted

Table 4
Comparison of the Molecular Mixing Ratio of CO_2 Under Various Conditions between the Model Simulation Results and the Experimental Results of Fleury et al. (2019) and Fleury et al. (2020)

	C/O = 1				C/O = 0.35			
	Thermal Only		Thermal + UV		Thermal Only		Thermal + UV	
	This Study	Exp. 2019[a]	This Study	Exp. 2019[b]	This Study	Exp. 2020[c]	This Study	Exp. 2020[c]
573 K	1.83×10^{-31}	1.50×10^{-5}	7.60×10^{-10}	1.00×10^{-3}	N/A			
873 K	4.96×10^{-17}	6.40×10^{-5}	4.56×10^{-10}	8.50×10^{-4}	N/A			
1173 K	6.88×10^{-14}	3.80×10^{-5}	5.33×10^{-11}	1.20×10^{-3}	1.08×10^{-5}	3.50×10^{-4}	1.08×10^{-5}	8.80×10^{-4}
1473 K	1.68×10^{-12}	3.40×10^{-5}	7.21×10^{-11}	4.30×10^{-4}	5.56×10^{-6}	3.60×10^{-4}	5.56×10^{-6}	5.60×10^{-4}

Notes.
[a] Mixing ratios of $^{13}CO_2$ taken from Table 2 in Fleury et al. (2019).
[b] Mixing ratios of $^{13}CO_2$ taken from Table 3 in Fleury et al. (2019).
[c] Mixing ratios of $^{13}CO_2$ taken from Table 3 in Fleury et al. (2020).

methane molecular mixing ratio at 1173 K is enough to be detected (i.e., $[CH_4] = 1.97 \times 10^{-8}$, which is around the same as the predicted mixing ratio of CH_4 plotted in Figure 6(a) at 1173 K with UV irradiation). However, it was surprising that no methane formation was observed in any of the experiments in Fleury et al. (2020). Two plausible explanations could be (i) errors in the current model overestimated the amount of CH_4 formation or (ii) a significant amount of H_2O included in the system from the beginning has disturbed the detection of any IR or mass-spectrometry peaks of CH_4 at 1173 K. With regard to (i), we can simply assess this by a sensitivity analysis. According to the sensitivity analysis, the most sensitive reaction and the most sensitive thermochemistry that affect the predicted formation of CH_4 is the reaction $CH_3 + OH \rightarrow CH_2OH + H$ and the thermochemistry of H_2 with their normalized sensitivities $\frac{d(\ln C_n)}{d(k_i)}$ of 0.5 and 1.25, respectively (see Figures C2(c) and (d) in Appendix C). This means that we have to reduce the rate coefficient of reaction (2) by 20 times or we have to reduce the Gibbs free energy of H_2 by 72% in order to decrease the predicted mixing ratio of CH_4 by 5 times. Although it is obvious that those parameters embed a certain amount of errors inside, it is less likely that these errors can solely explain the non-detection of CH_4 in Fleury et al. (2020). Rather, it would be more reasonable to lean to explanation (ii) (i.e., interference on the IR peaks and mass-spec peaks of CH_4 due to a significant amount of preexisting H_2O in their experimental condition of Fleury et al. 2020). Other than that, the current model's reaction kinetic interpretation qualitatively matches well with the experimental observation of Fleury et al. (2020).

3.5. Quantitative Comparison of the Mixing Ratio of CO_2 between the Model Simulation Results and the Experimental Results of Fleury et al. (2019) and Fleury et al. (2020)

Since Fleury et al. (2019, 2020) quantified the mixing ratios of CO_2 under various experimental conditions using the Beer–Lambert law on the IR spectroscopy results, we tried to derive some quantitative comparisons of CO_2 between the model simulation results and the experimental results under their corresponding experimental conditions. Although the discrepancy between the model simulation results and the experimental results of the C/O = 0.35 condition is within 2 orders of magnitude as shown in Table 4, the discrepancy between the model simulation results and the experimental results of the C/O = 1 condition is significantly larger compared to the discrepancy in the C/O = 0.35 condition. There are multiple factors that can derive this discrepancy. First, as mentioned in the main text, the products that are observed in gas-phase static cell experiments conducted by Fleury et al. (2019, 2020) are formed far beyond tertiary or even further reaction chemistry including surface chemistry on the wall since these experiments were conducted for more than 18 hr. Surface chemistry is considered to be more efficient and faster compared to gas-phase chemistry and very difficult to simulate in detail. Although surface chemistry is indeed very important when it comes to precisely describing the experimental study, it was beyond the scope of the current work to gain a better insight into simultaneous thermally and photochemically driven reaction pathways involving electronically excited CO in its metastable state ($a^3\Pi$). Natural isotopic contamination when using enriched isotopic gases was mentioned in Fleury et al. (2019) and affected the chemistry, which might have led to the discrepancy as well. The calculation of the absorption cross section of CO_2 described in Section 2.5 in Fleury et al. (2019) can also affect the discrepancy as well. We conclude it is likely that the discrepancy is mainly due to the combined effects of the multiple factors mentioned above as well as experimental uncertainties. As mentioned earlier, the quantitative discrepancy does not indicate a fundamental issue with the reaction kinetic model, but rather reflects our imperfect knowledge of the values of the model parameters.

Keeping the quantitative comparison aside, which can be influenced by the experimental conditions discussed above, our modeling work clearly predicts the experimental observations (a) for C/O = 1, where only H_2 and CO molecules were present in the beginning, and the thermochemical formation of CO_2 is significantly less efficient than thermally augmented photochemical production of CO_2, as observed by Fleury et al. (2019); (b) for C/O = 0.35, which was achieved through the addition of H_2O to the H_2 + CO starting composition, the chemistry is mainly driven by the H_2O dissociation (both thermally and photochemically) and no significant difference is observed between thermal and thermally augmented photochemical reaction pathways as a result. Our model again confirms the experimental observations of Fleury et al. (2020).

This analysis also highlights the importance of both experimental work and rigorous modeling of theoretical reaction kinetics. Further, this work confirms that though experimental conditions have limitations that are unavoidable (such as reaction cell boundaries), the relative equilibrium mixing ratios obtained from the experiments are similar to the predicted ones.

3.6. Impact of the Current Study on the Field of Astrochemistry

In this work, we have implemented a state-of-the-art computer-aided automatic construction of an astrochemical reaction network and successfully demonstrated how this computer-aided reaction kinetic model can help us precisely interpret the previous photochemical experiment in detail. Not only have we figured out the photochemically important role of the UV-excited state of carbon monoxide, but we also suggest future studies such as the measurement of the temperature dependency of the cross sections of carbon monoxide or the experiment and modeling combined kinetic study of C_2H_2-UV photochemistry. Our work clearly demonstrates the importance of coupling photochemical reaction pathways to thermochemical models to better understand exoplanet atmospheres. Only then will we be able to realistically describe the atmospheric chemistry of exoplanets that receive a significant amount of UV photons from their parent stars. JWST transmission spectroscopy data will keep providing us with a deluge of exoplanetary data that need to be efficiently and precisely interpreted by atmospheric chemical models. As we can see from the case of the recent study by Tsai et al. (2022), it is important to properly implement photochemical reactions in chemical models to properly interpret observational data and extract valuable insight into exoplanet atmospheres. We hope our study will be the benchmark for future studies of exoplanet atmospheric photochemical modeling that will consequently lead to rapid innovation in the field of astrochemistry.

4. Conclusions

In this work, we utilized an automatic chemical reaction mechanism generator to build a large and complex thermo- and photochemical network that can qualitatively rationalize the augmented chemistry observed from previous experimental works by Fleury et al. (2019, 2020). Our model has demonstrated that Lyα-aided electronically excited carbon monoxide in its metastable state ($a^3\Pi$) can significantly enhance the chemistry in the exoplanet atmosphere-like conditions through two different reactions, which are (i) H_2 + $CO(a^3\Pi) \rightarrow H + HCO$ and (ii) $CO(X^1\Sigma^+) + CO(a^3\Pi) \rightarrow CO_2 + C(^3P)$. The first reaction (i.e., $H_2 + CO(a^3\Pi) \rightarrow H + HCO$) leads to the significantly augmented formation of HCO radicals in a H_2-dominated system, which can push the whole chemistry to further CH_4, H_2O, and CO_2 formation even at a very low temperature of 573 K. At temperatures above 873 K, the second reaction (i.e., $CO(X^1\Sigma^+) + CO(a^3\Pi) \rightarrow CO_2 + C(^3P)$) forms CO_2 and the triplet C radicals that rapidly hydrogenate into CH_4, which mainly contributes to the significantly augmented formation of major species. However, at temperatures above 2000 K, thermal chemistry then becomes efficient enough to dominate the whole chemistry. Given the experimental conditions of Fleury et al. (2019, 2020), the transition temperature in which thermal chemistry becomes dominant compared to photochemistry starts at ~1970 K, and this transition temperature can be shifted due to multiple factors. Finally, under the experimental conditions of Fleury et al. (2019, 2020), our model might suggest that thermal-only chemistry up to 2500 K cannot push the chemistry to larger species such as PAHs or even organic aerosols, and instead, C_2H_2 photochemistry and the photochemistry of higher carbon species that are produced from C_2H_2 photochemistry might be the key to explaining the experimentally observed hydrocarbon aerosol formations observed from the previous experiments by Fleury et al. (2019). The model results have demonstrated the importance of electronically excited metastable carbon monoxide in exoplanet atmospheres and that adding more photochemical reactions and species to current 1D photochemical models would provide a more comprehensive understanding of exoplanet atmospheres.

This research work was carried out at the Jet Propulsion Laboratory, California Institute of Technology, under a contract with the National Aeronautics and Space Administration. This research work was funded by the NASA Exoplanet Research Program grant to M.S.G. B.F. thanks the Université Paris-Est Créteil (UPEC) for funding support (postdoctoral grant).

Appendix A
ROP Analysis

In this section, the ROP analysis data are provided. Every table contains the rate of production of two species under two different conditions (i.e., the thermal-only condition and the thermal- and UV-combined condition). Each row represents the corresponding time and each column represents the corresponding condition. The units are in mol m^{-3} s^{-1}. For example, in the second row of the left side of Figure A1(f), one can see the rate of formation of CO_2 at the reaction time of 100 μs (10^{-4} s) under two different conditions (i.e., the thermal-only condition and the thermal- and UV-combined condition). It can be seen that at 100 μs under the thermal-only condition at 573 K, CO_2 is mainly formed through OH + CO $\leftrightarrow$ H + CO_2. However, it has to be noted that the rate of production through this reaction is almost insignificant (i.e., ~10^{-44} mol m^{-3} s^{-1}) at 100 μs. In contrast to this, with UV at 573 K, CO_2 is efficiently formed through CO + $CO(a^3\Pi) \leftrightarrow C + CO_2$ with the production rate of 10^{-16} mol m^{-3} s^{-1} at 100 μs, which demonstrates the importance of the CO photochemistry in the system as mentioned in the main text. Figures A2–A4 refer to the ROP analysis of corresponding temperature condition of the system of Fleury et al. (2019).

(a)

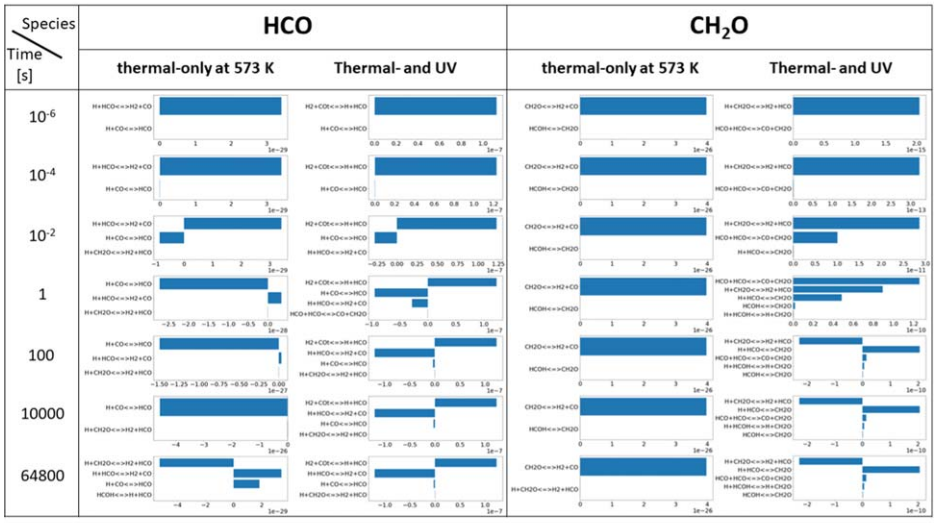

(b)

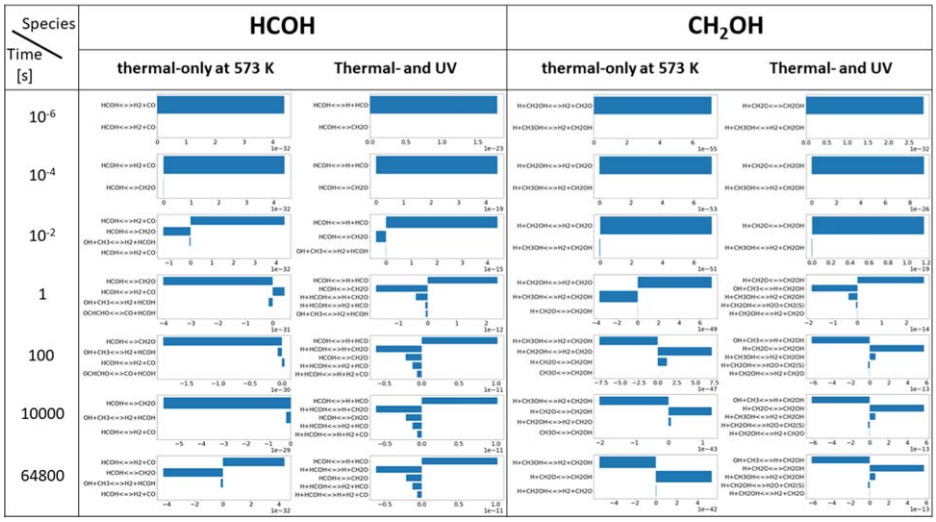

(c)

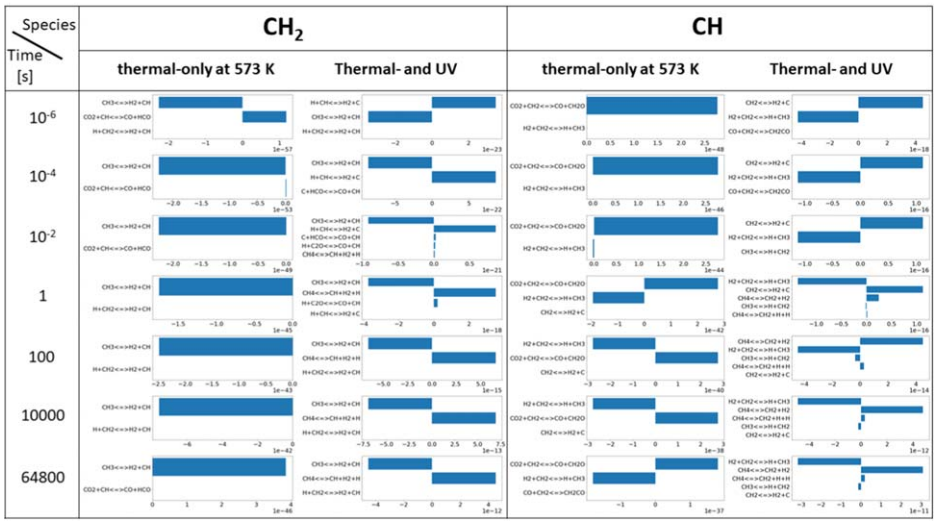

Figure A1. Analysis of the rate of production of each species: (a) HCO and CH_2O; (b) HCOH and CH_2OH; (c) CH_2 and CH; (d) CH_3 and OH; (e) CH_4 and H_2O; and (f) CO_2 and C_2H_2 at temperatures of 573 K of the system of Fleury et al. (2019). Each row represents the corresponding time and each column represents the corresponding condition (i.e., thermal only or thermal and UV photochemistry). The numbers in the figure are in units of mol m^{-3} s^{-1}.

(d)

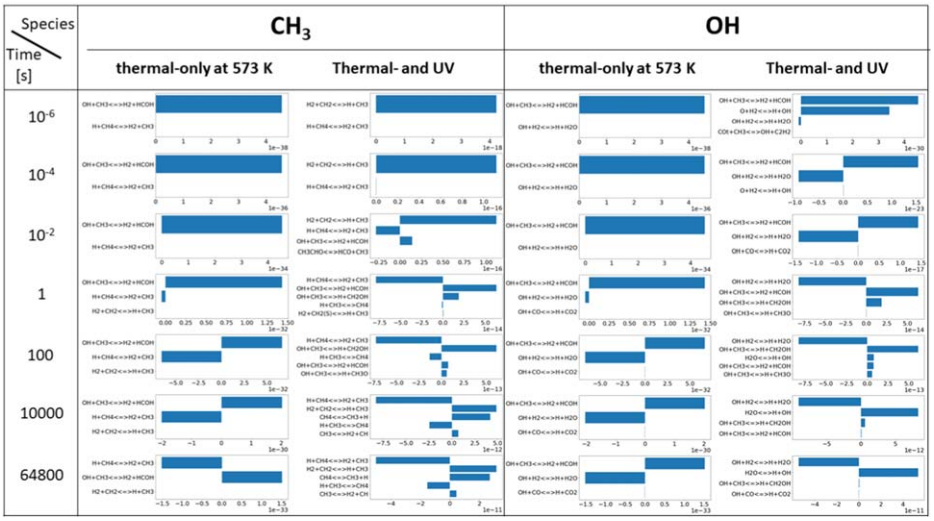

(e)

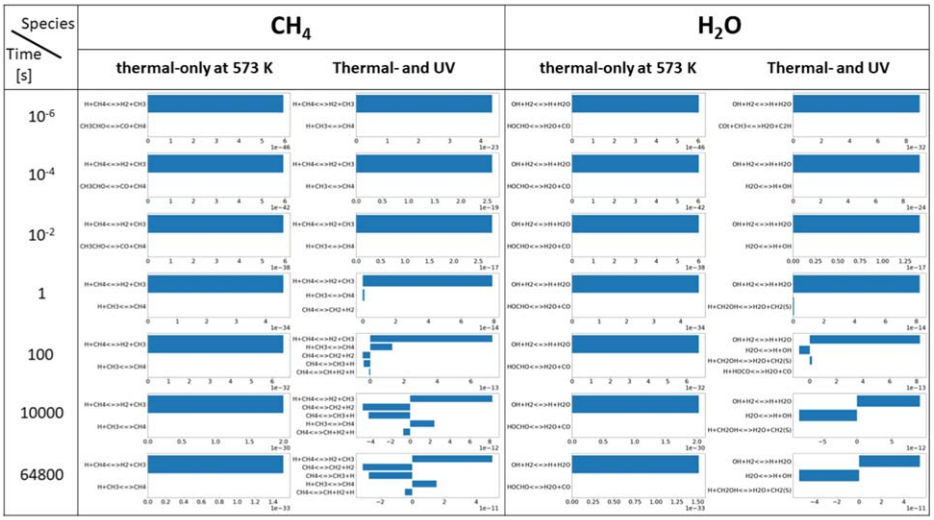

(f)

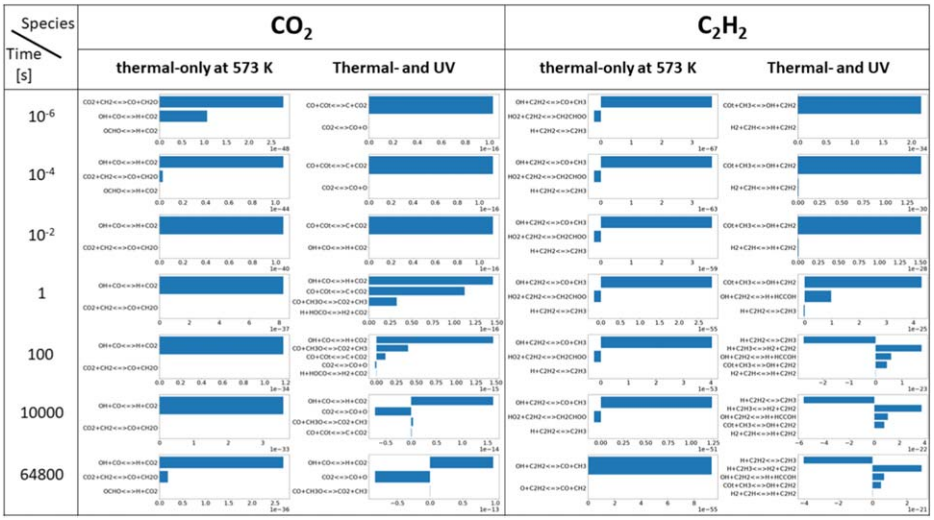

Figure A1. (Continued.)

(a)

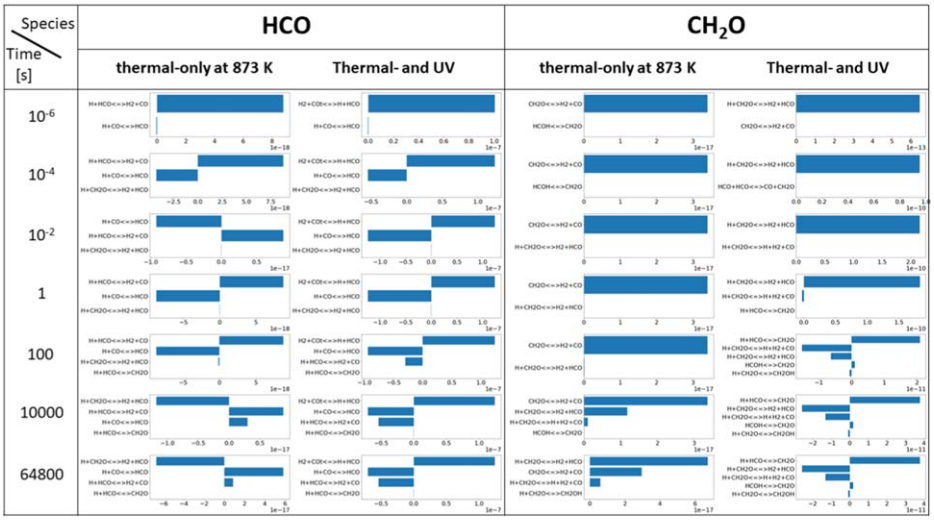

(b)

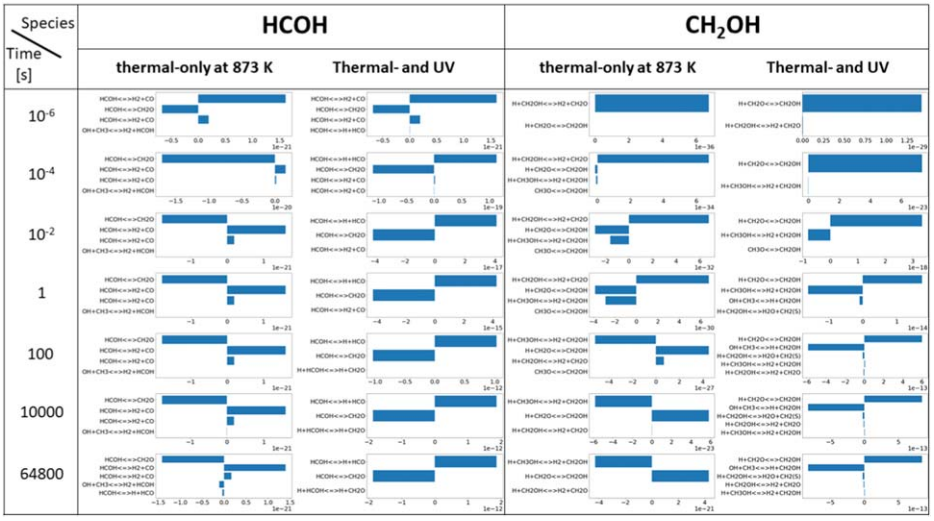

(c)

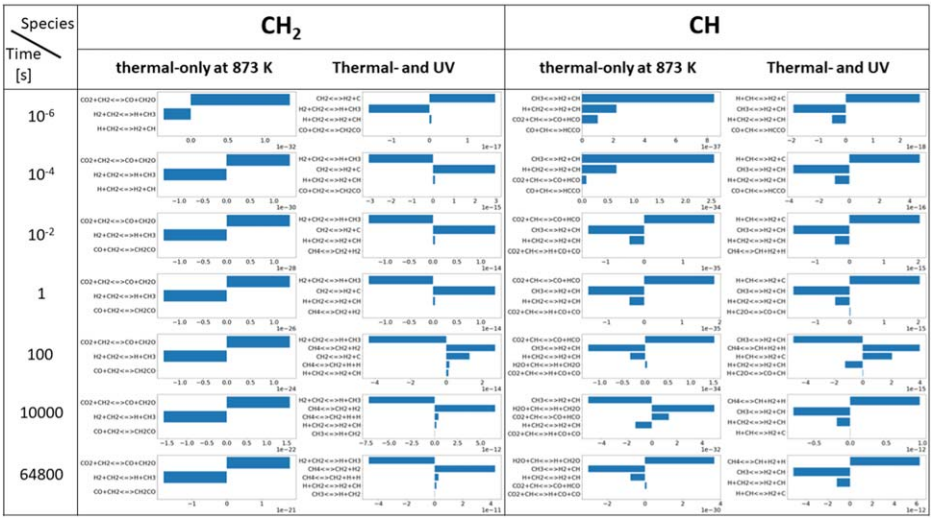

Figure A2. Analysis of the rate of production of each species: (a) HCO and CH_2O; (b) HCOH and CH_2OH; (c) CH_2 and CH; (d) CH_3 and OH; (e) CH_4 and H_2O; and (f) CO_2 and C_2H_2 at temperatures of 873 K of the system of Fleury et al. (2019). Each row represents the corresponding time and each column represents the corresponding condition (i.e., thermal only or thermal and UV photochemistry). The numbers in the figure are in units of mol m^{-3} s^{-1}.

(d)

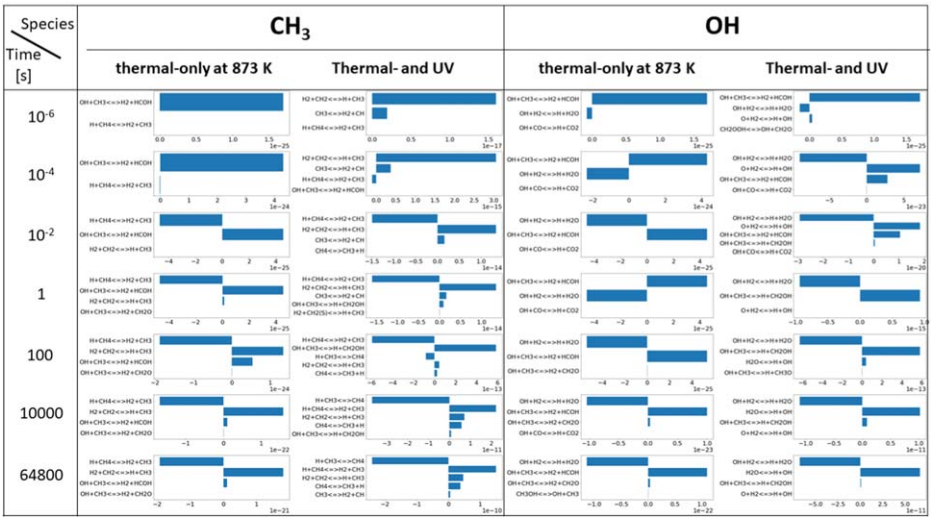

(e)

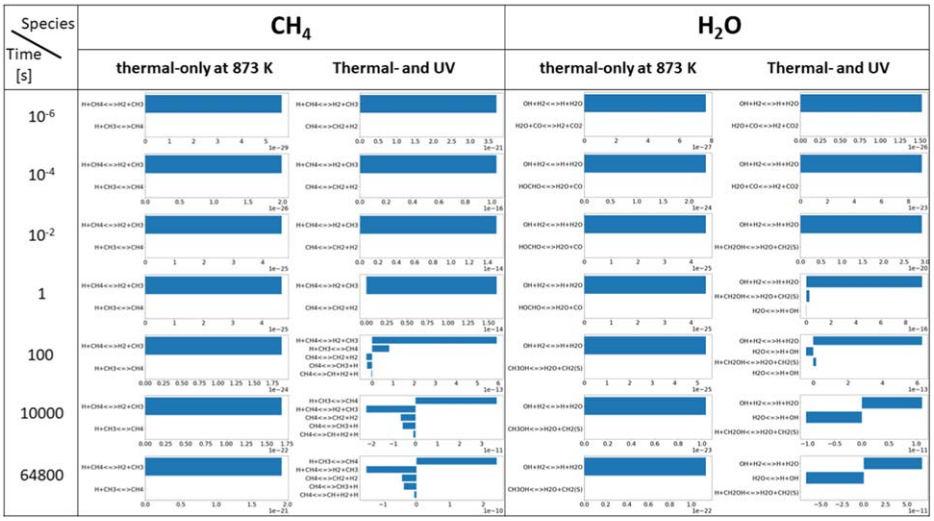

(f)

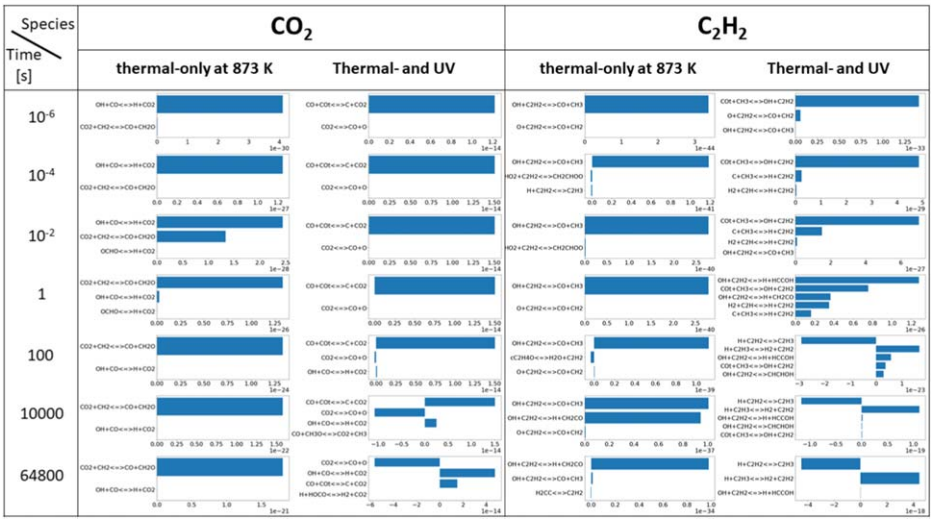

Figure A2. (Continued.)

(a)

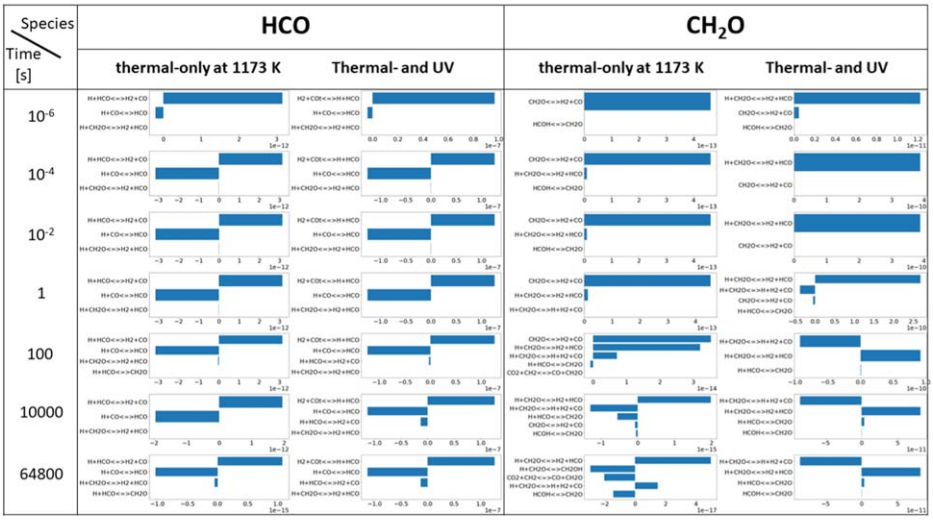

(b)

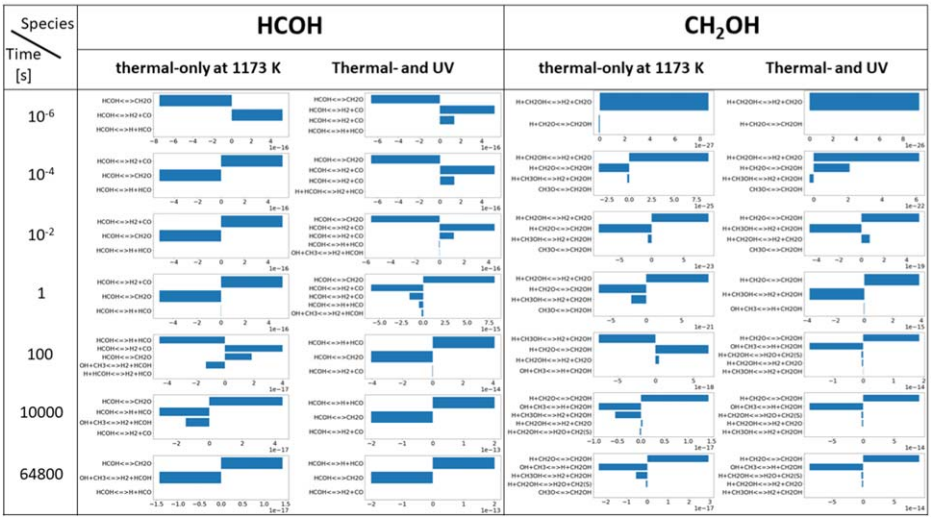

(c)

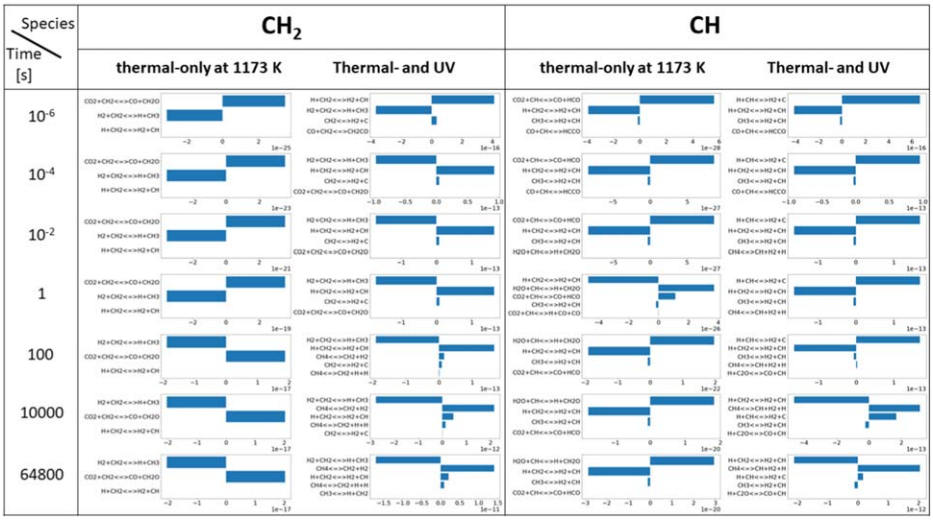

Figure A3. Analysis of the rate of production analysis of each species: (a) HCO and CH_2O; (b) HCOH and CH_2OH; (c) CH_2 and CH; (d) CH_3 and OH; (e) CH_4 and H_2O; and (f) CO_2 and C_2H_2 at temperatures of 1173 K of the system of Fleury et al. (2019). Each row represents the corresponding time and each column represents the corresponding condition (i.e., thermal only or thermal and UV photochemistry). The numbers in the figure are in units of mol m^{-3} s^{-1}.

(d)

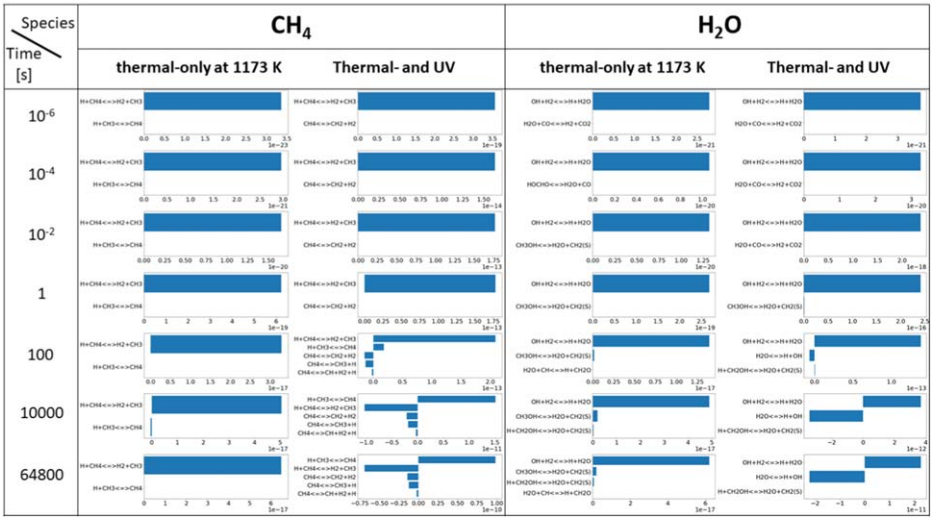

(e)

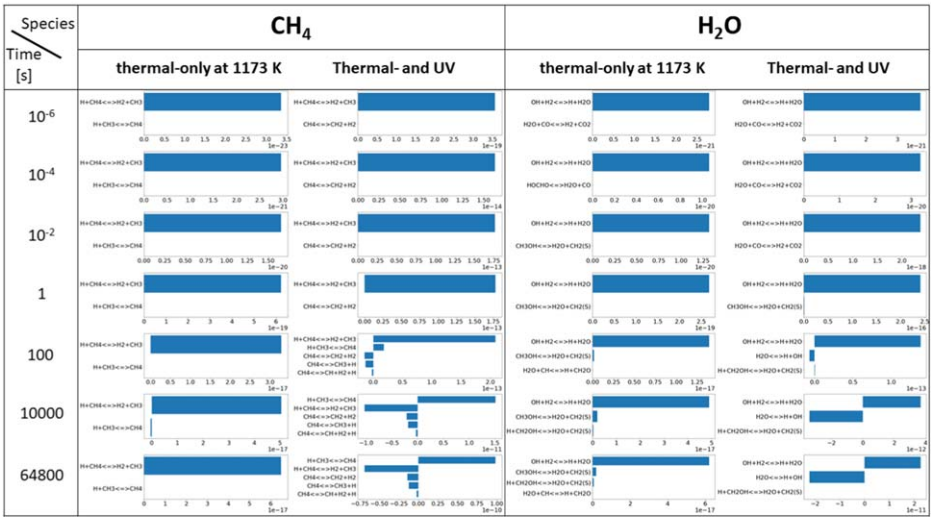

(f)

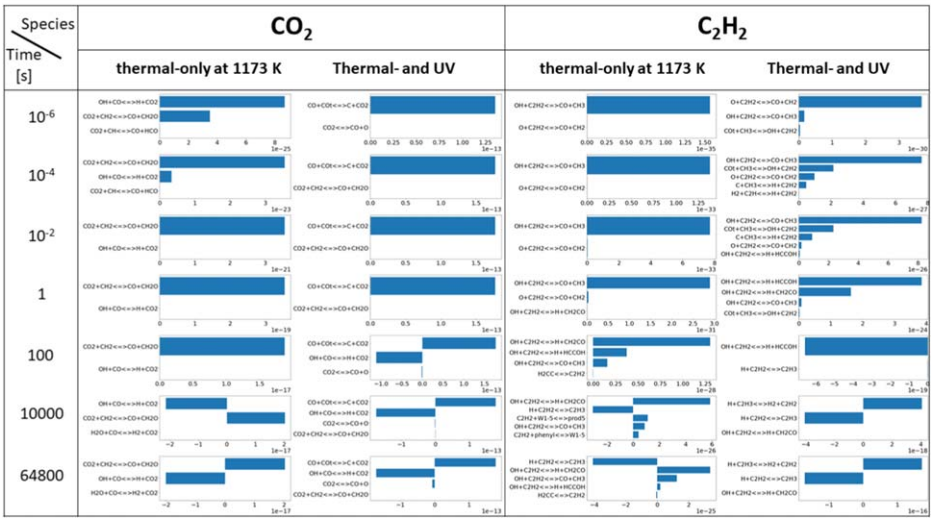

Figure A3. (Continued.)

(a)

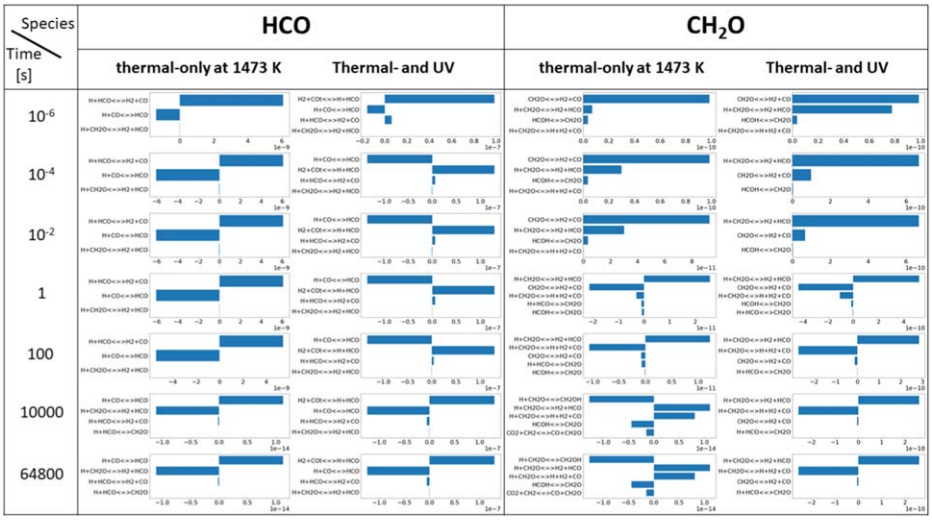

(b)

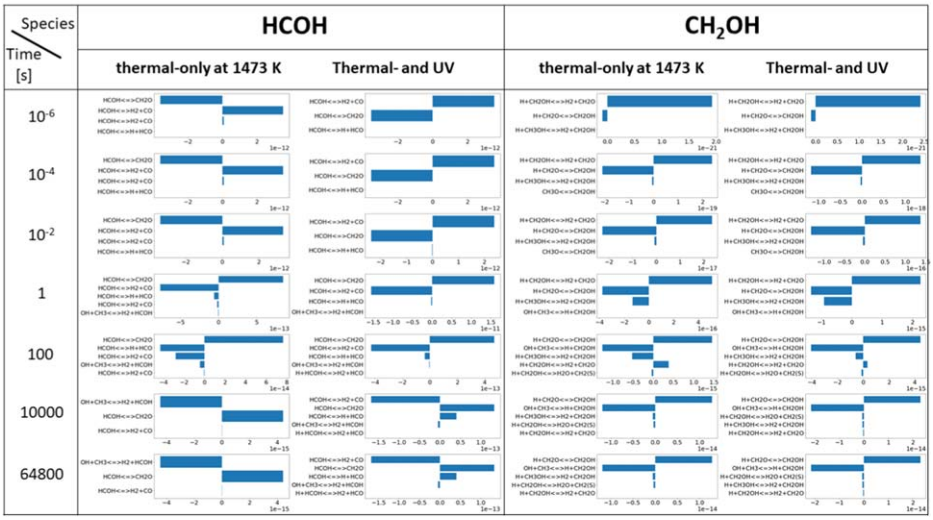

(c)

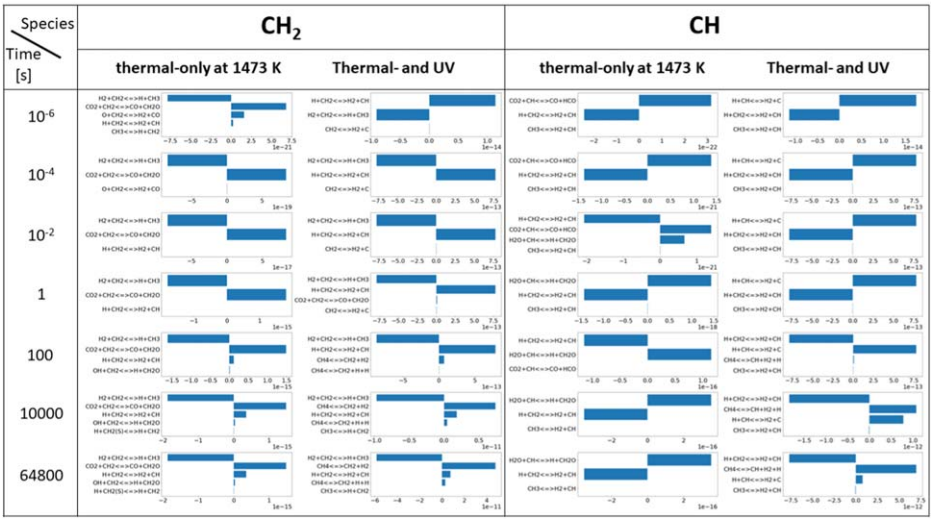

Figure A4. Analysis of the rate of production of each species: (a) HCO and CH_2O; (b) HCOH and CH_2OH; (c) CH_2 and CH; (d) CH_3 and OH; (e) CH_4 and H_2O; and (f) CO_2 and C_2H_2 at temperatures of 1473 K of the system of Fleury et al. (2019). Each row represents the corresponding time and each column represents the corresponding condition (i.e., thermal only or thermal and UV photochemistry). The numbers in the figure are in units of mol m^{-3} s^{-1}.

(d)

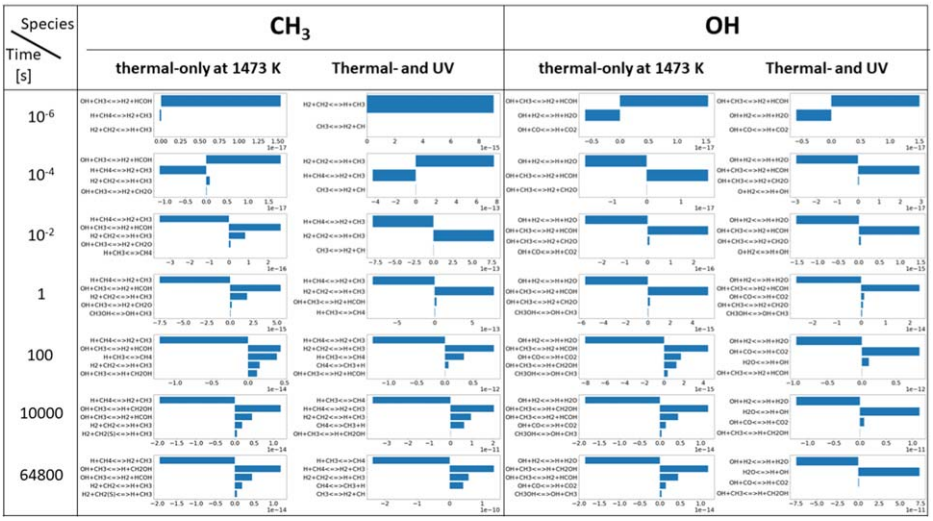

(e)

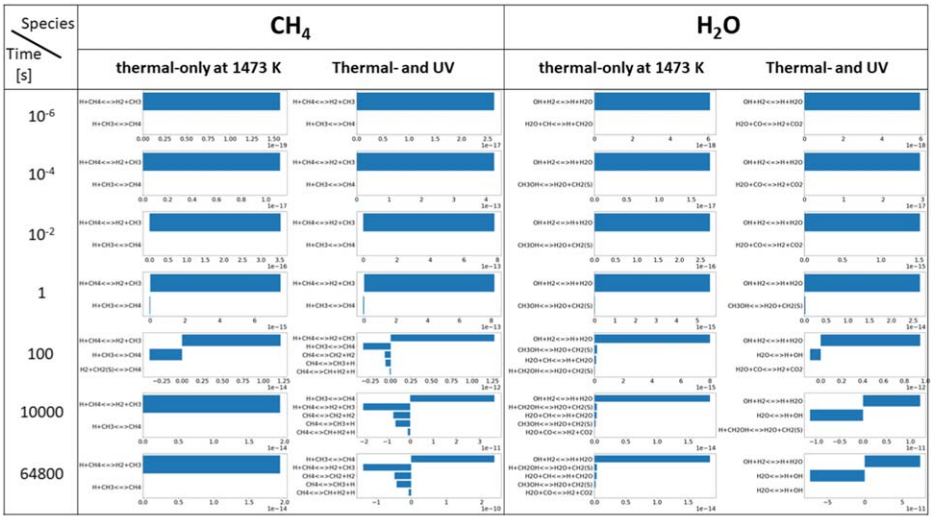

(f)

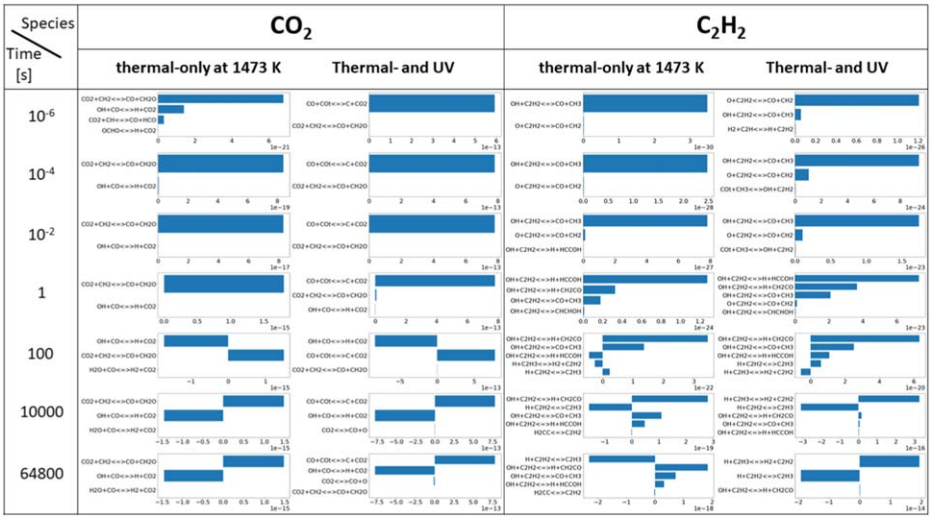

Figure A4. (Continued.)

Appendix B
Time-dependent Mole-fraction Profiles of C_2H_2 Under Various Experimental Conditions

Figure B1 shows the time-dependent molecular mixing ratio profiles of acetylene predicted by the kinetic model under various experimental conditions with UV photons available.

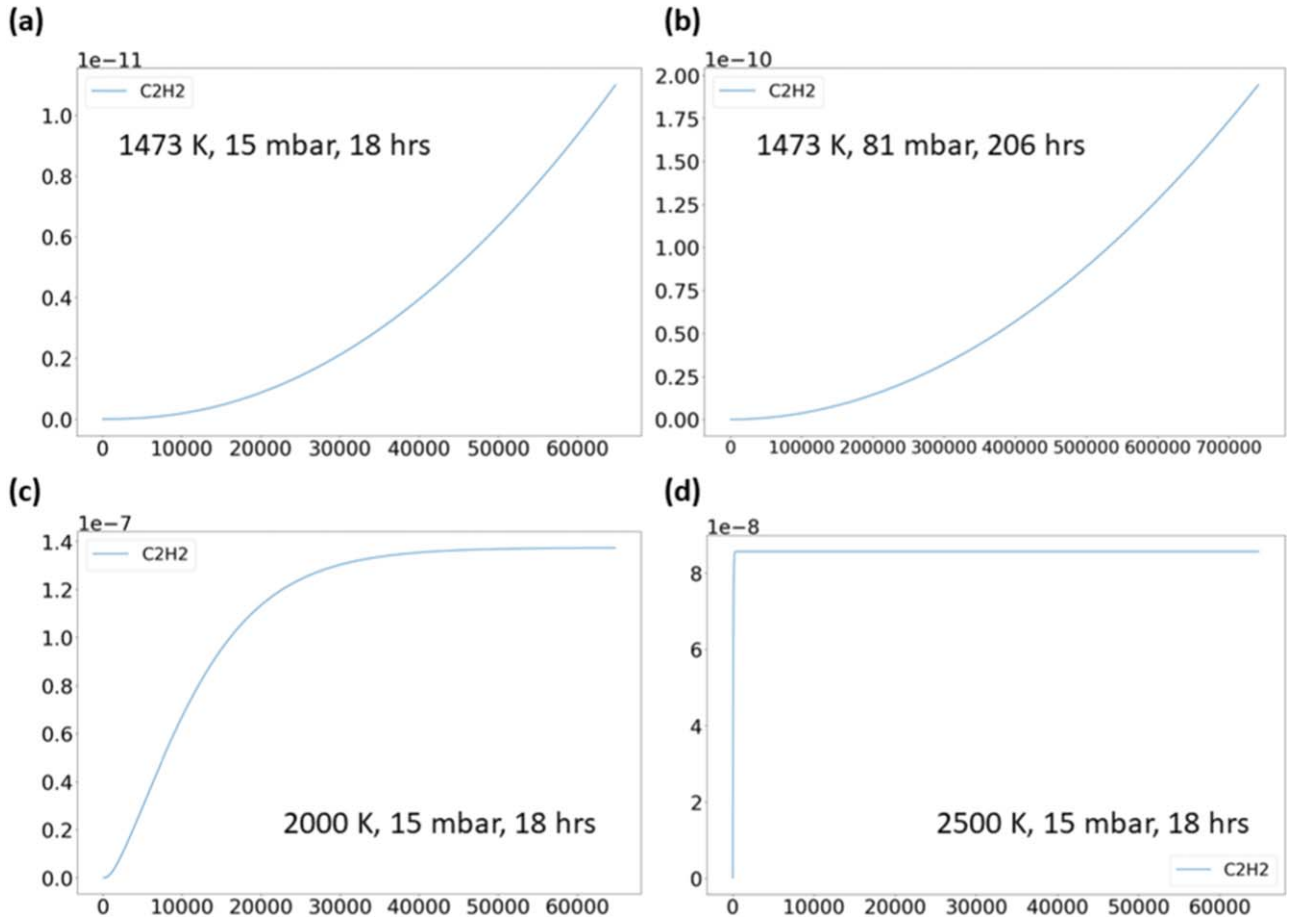

Figure B1. Time-dependent (the unit of the *x*-axis is [s]) molecular mixing ratio profiles of acetylene predicted by the kinetic model under various experimental conditions with UV photons available (initial mole fractions of H_2:CO = 99.7:0.3): (a) 1473 K, 15 mbar, 18hr; (b) 1473 K, 81 mbar, 206 hr; (c) 2000 K, 15 mbar, 18 hr; (d) 2500 K, 15 mbar, 18 hr.

Appendix C
Sensitivity Analysis

Figure C1 shows the sensitivity analysis of the kinetic model that simulated 1473 K and 15 mbar experimental condition of Fleury et al. (2019). Figure C2 shows the sensitivity analysis of the kinetic model that simulated 1473 K and 15 mbar experimental condition of Fleury et al. (2020).

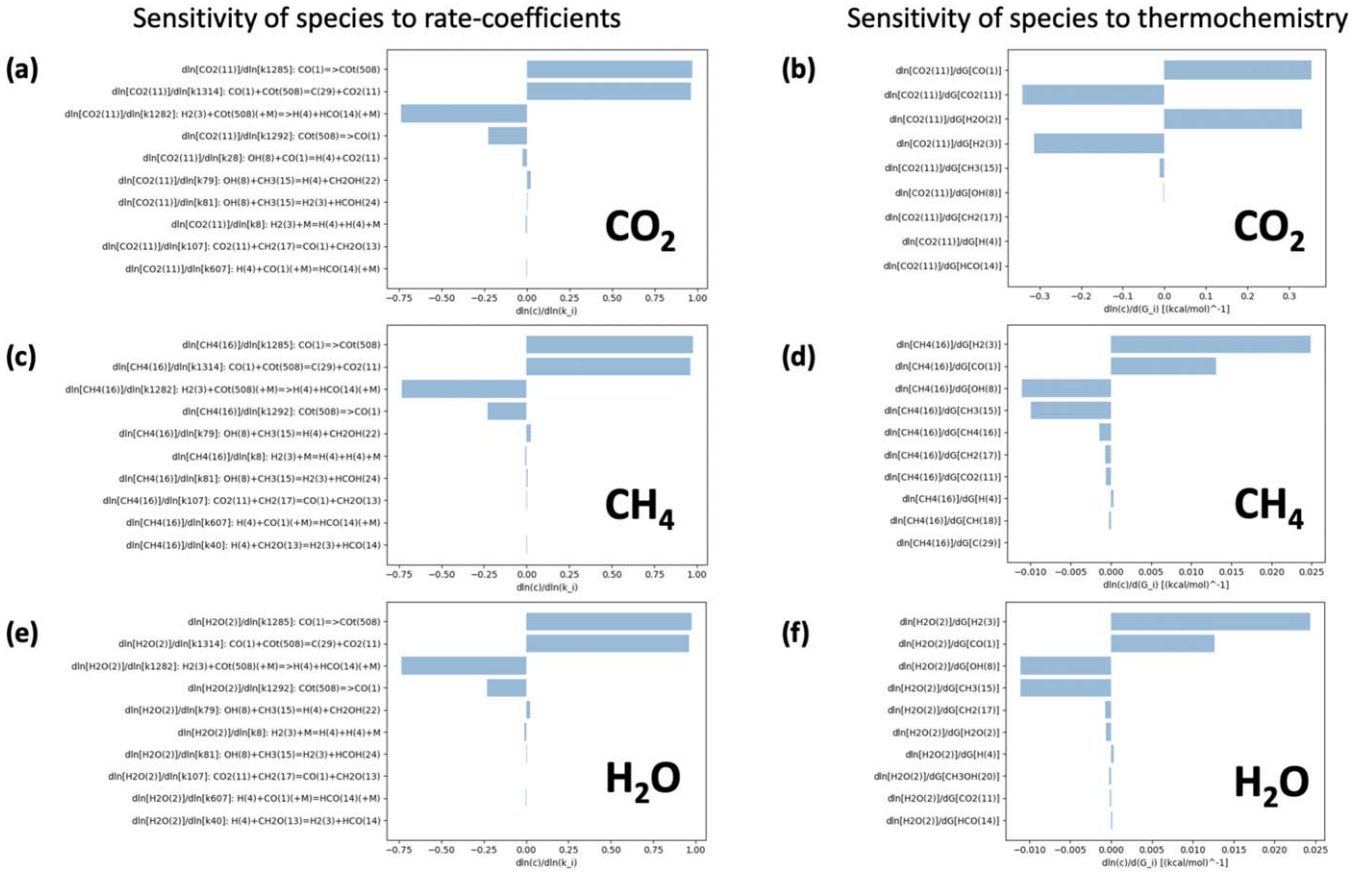

Figure C1. Analysis of the sensitivity of (a) CO_2 to rate coefficients; (b) CO_2 to thermochemistry; (c) CH_4 to rate coefficients; (d) CH_4 to thermochemistry; (e) H_2O to rate coefficients; (f) H_2O to thermochemistry; simulated under the condition of 1473 K, 15 mbar, $[H_2] = 0.997$, $[CO] = 0.003$.

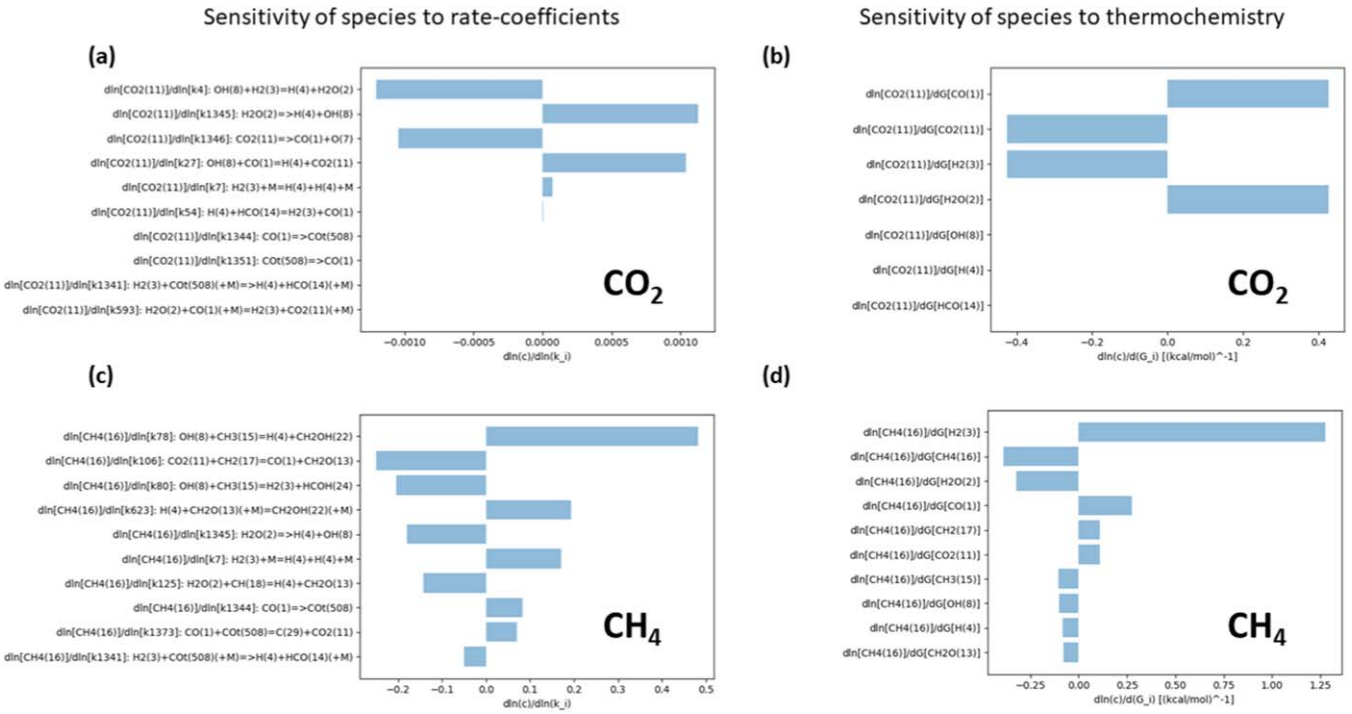

Figure C2. Analysis of the sensitivity of(a) CO_2 to rate coefficients; (b) CO_2 to thermochemistry; (c) CH_4 to rate coefficients; (d) CH_4 to thermochemistry; simulated under the condition of 1473 K, 15 mbar, $[H_2] = 0.9926$, $[CO] = 0.0026$, $[H_2O] = 0.0034$.

Appendix D
Time-dependent Mole-fraction Profiles of CO_2 Under Various Experimental Conditions

Figure D1 shows the kinetic model-simulated time-dependent molecular mixing ratio profile of CO_2 under various conditions of Fleury et al. (2020).

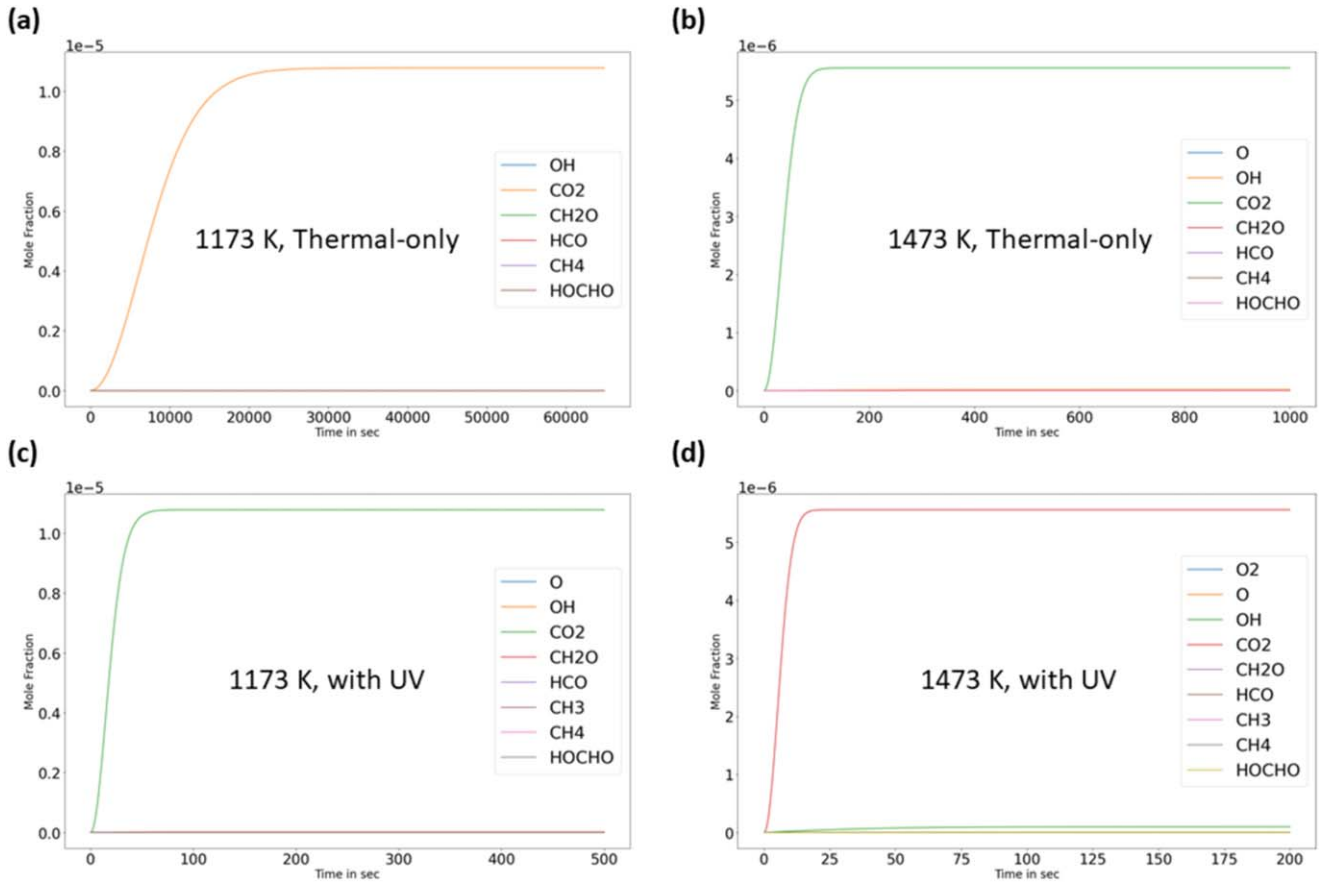

Figure D1. Simulated time-dependent molecular mixing ratio profile of CO_2 under the various conditions of Fleury et al. (2020): (a) 1173 K, thermal only; (b) 1473 K, thermal only; (c) 1173 K, with UV irradiation; (d) 1473 K, with UV irradiation; all simulated under the condition of 15 mbar, $[H_2] = 0.9926$, $[CO] = 0.0026$, $[H_2O] = 0.0034$.

ORCID iDs

Jeehyun Yang https://orcid.org/0000-0002-1551-2610
Murthy S. Gudipati https://orcid.org/0000-0001-5992-373X
Bryana L. Henderson https://orcid.org/0000-0001-9385-3376
Benjamin Fleury https://orcid.org/0000-0003-1845-6690

References

Allen, J. W., Goldsmith, C. F., & Green, W. H. 2012, PCCP, 14, 1131
Backx, C., Wight, G. R., & Van der Wiel, M. J. 1976, JPhB, 9, 315
Bittner, J. D., & Howard, J. B. 1981, Symp. (Int.) Combust., 18, 1105
Brem, B. T., Durdina, L., Siegerist, F., et al. 2015, EnST, 49, 13149
Chu, T.-C., Buras, Z. J., Smith, M. C., Uwagwu, A. B., & Green, W. H. 2019, PCCP, 21, 22248
DeVine, J. A., Choudhury, A., Lau, J. A., Schwarzer, D., & Wodtke, A. M. 2022, JPCA, 126, 2270
Drummond, B., Carter, A. L., Hebrard, E., et al. 2019, MNRAS, 486, 1123
Euclides, H. O., & Barreto, P. R. P. 2019, J. Mol. Model., 25, 1
Fleury, B., Gudipati, M. S., Henderson, B., & Swain, M. 2019, ApJ, 871, 158
Fleury, B., Gudipati, M. S., Henderson, B., & Swain, M. 2020, ApJ, 899, 147
Fournier, J., Mohammed, H. H., Deson, J., Vermeil, C., & Schamps, J. 1980, JChPh, 73, 6039
France, K., Froning, C. S., Linsky, J. L., et al. 2013, ApJ, 763, 149
Franklin, J. P. 2018, PhD thesis, Massachusetts Institute of Technology
Frenklach, D. W., Clary, D. W., Gardiner, W. C., & Stein, S. E. 1985, Symp. (Int.) Combust., 20, 887
Frenklach, M., & Mebel, A. M. 2020, PCCP, 22, 5314
Frisch, M. J., Trucks, G. W., Schlegel, H. B., et al. 2009, Gaussian 09 Revision E.01, https://gaussian.com/g09citation/
Gans, B., Boye-Peronne, S., Broquier, M., et al. 2011, PCCP, 13, 8140
Gao, C. W., Allen, J. W., Green, W. H., & West, R. H. 2016, CoPhC, 203, 212
Golan, A., Ahmed, M., Mebel, A. M., & Kaiser, R. I. 2013, PCCP, 15, 341
Gudipati, M. S., & Kalb, M. 1998, A&A, 329, 375
Hashemi, H., Christensen, J. M., Gersen, S., et al. 2016, CoFl, 172, 349
Hu, R., Seager, S., & Bains, W. 2012, ApJ, 761, 166
Jasper, A. W., Oana, C. M., & Miller, J. A. 2015, Proc. Combust. Inst., 35, 197
Johnson, M. S., Pang, H., Dong, X., & Green, W. H. 2019, Reaction Mechanism Simulator, https://reactionmechanismgenerator.github.io/ReactionMechanismSimulator.jl/latest/
Laufer, A. H., & McNesby, J. R. 1965, CaJCh, 43, 3487
Lee, R. A., Ajello, J. M., Malone, C. P., et al. 2020, JGRE, 126, e06602
Ligterink, N. F. W., Paardekooper, D. M., Chuang, K. J., et al. 2015, A&A, 584, A56
Liu, M., Chu, T.-C., Jocher, A., et al. 2020, Int. J. Chem. Kinet., 53, 27
Liu, M., Grinberg, A. D., Johnson, M. S., et al. 2021, J. Chem. Inf. Model., 61, 2686
Madhusudhan, N., Agúndez, M., Moses, J. I., & Hu, Y. 2016, SSRv, 205, 285
Madhusudhan, N. 2012, ApJ, 758, 36
Marcus, R. A. 1952, JChPh, 20, 359
Miguel, Y., Kaltenegger, L., Linsky, J. L., & Rugheimer, S. 2015, MNRAS, 446, 345
Miller, J. A., & Klippenstein, S. J. 2006, JPCA, 110, 10528
Miller, J. A., & Melius, C. F. 1989, Symp. (Int.) Combust., 21, 1031
Moses, J. I. 2014, RSPTA, 372, 20130073
Moses, J. I., Madhusudhan, N., Visscher, C., & Freedman, R. S. 2013, ApJ, 763, 25
Moses, J. I., Visscher, C., Fortney, J. J., et al. 2011, ApJ, 737, 15
Mota, R., Parafita, R., Giuliani, A., et al. 2005, CPL, 416, 152
Mount, G. H., Warden, E. S., & Moos, H. W. 1977, ApJ, 214, L47
Myer, J. A., & Samson, J. A. R. 1970, JChPh, 52, 266
Norinaga, K., Janardhanan, V. M., & Deutschmann, O. 2008, Int. J. Chem. Kinet., 40, 199
Parker, D. S. N., Kaiser, R. I., Troy, T. P., & Ahmed, M. 2014, Angew. Chem., Int. Ed., 53, 7740
Roudier, G. M., Swain, M. R., Gudipati, M. S., et al. 2021, AJ, 162, 37
Smith, M. C., Zhu, G., Buras, Z. J., et al. 2020, JPCA, 124, 2871
Thompson, B. A., Harteck, P., & Reeves, R. R., Jr. 1963, JGR, 68, 6431
Trainer, M. G., Sebree, J. A., Yoon, Y. H., & Tolbert, M. A. 2013, ApJL, 766, L4
Tsai, S.-M., Lee, E. K. H., Powell, D., et al. 2022, Natur, in press (arXiv:2211.10490)
Venot, O., Bénilan, Y., Fray, N., et al. 2018, A&A, 609, A34
Venot, O., Hébrard, E., Agúndez, M., et al. 2012, A&A, 546, A43
Venot, O., Hébrard, E., Agúndez, M., Decin, L., & Bounaceur, R. 2015, A&A, 577, A33
Yang, T., Troy, T. P., Xu, B., et al. 2016, Angew. Chem., Int. Ed., 55, 14983